Science Advances
AAAS

Supplementary Materials for

A machine-learning–powered spectral-dominant multimodal soft wearable system for long-term and early-stage diagnosis of plant stresses

Qin Jiang *et al.*

Corresponding author: Xiaodong Chen, chenxd@ntu.edu.sg; Zhigang Wu, zgwu@hust.edu.cn

Sci. Adv. **11**, eadw7279 (2025)
DOI: 10.1126/sciadv.adw7279

The PDF file includes:

Other Supplementary Material for this manuscript includes the following:

Note S1. Theoretical deduction of the relationship between *Tr* and *ΔH*.

As shown in **fig. S13a**, a commercial plant transpiration meter is used to place the tested leaf in a sealing chamber to measure the leaf transpiration rate (*Tr,* mol m^{-2} s^{-1}). In this open system, the *Tr* equals the additional amount of water vapor leaving the chamber above that entering. Therefore, the water vapor produced by the leaf via transpiration is given as(*70*),

$$Tr = \frac{u_e(w_o - w_e)}{s(1-w_o)},$$

where w_e and w_o (mol mol^{-1}) are the mole fractions of water vapor (mol of water vapor per total of all gases) in the entering and outgoing air streams, respectively, *s* (m^2) is the leaf area, and u_e (mol s^{-1}) is the total molar flow rate (air plus water vapor) entering the chamber, respectively.

According to Dalton's law of partial pressures, which states that the mole fraction of a gas in a mixture is equal to its partial pressure, w_e and w_o can be calculated from measurements of relative humidity (*H*, % RH), as in the following equation,

$$w = H\left(\frac{v_{w,sat}}{P \times 100}\right),$$

where $v_{w,sat}$ is the saturation water vapor pressure at the temperature of the humidity sensor, *P* is the total air pressure at the humidity sensor. Therefore, the water vapor gradient (Δw) between the entering (w_e) and outgoing (w_o) of the chamber is a positive correlation with the humidity difference (ΔH) between the inlet air humidity (H_{inlet}) and the outlet air humidity (H_{outlet}), as in the following equation,

$$\Delta w = (\mathrm{w_e} - \mathrm{w_o}) \propto \Delta H = (H_{outlet} - H_{inlet}).$$

Therefore, the equation of Tr can be rearranged as,

$$Tr = \gamma \frac{u_e \Delta H}{s},$$

where γ is a correction factor. As the u_e and *s* is constant during the transpiration measurement, the Tr is theoretically determined by the ΔH.

In our design, the soft sensor patch was attached to the leaf's epidermis to form a gap chamber for collecting the variation of leaf humidity (H_{leaf}) via its T&H sensor, as shown in **fig. S13b**. Also, the environment humidity (H_{env}) is recorded by the T&H sensor located on the FPCB. Therefore, according to the above theory deduction, the Tr is theoretically related to the humidity difference (*ΔH*) between the H_{leaf} and H_{env}, which can be expressed as,

$$Tr \propto \Delta H = H_{leaf} - H_{env}.$$

Briefly, this principle presents a new indicator for measuring leaf transpiration rate (Tr) by recording in-situ leaf humidity (H_{leaf}) and environmental humidity (H_{env}).

Note S2. Workflow of the ML-powered diagnostic framework

To comprehensively analyze real-time T&H and spectral data from the leaf and surrounding environment, we designed an ML-powered diagnostic framework, consisting of the THD and SDM (**fig. S14**). The framework operates in two stages for analyzing multimodal sensor information as follows.

In Stage 1, the THD was used to identify outliers in T&H data of leaves and the environment caused by heat, drought, and senescent conditions. The regulations are set as follows.

(1) If the leaf temperature (T_{leaf}) or the environmental temperature (T_{env}) exceeds 35℃, the THD will assess that the plant is under heat stress, reminding researchers to cool down the cultivation environment.

(2) The maximum humidity difference (ΔH_{max}) within a day can be calculated as,

$$\Delta H_{max} = max\{H_{leaf} - \Delta H_{env}\}.$$

Therefore, if the ΔH_{max} is lower than 10% RH, the THD will first diagnose that the plant is under drought stress and remind researchers to water the plant. Subsequently, if the ΔH_{max} remains at a low level on the following day, the THD would diagnose the tested leaf as undergoing a senescent process.

Until T&H data are determined to be within normal ranges, the framework proceeds to Stage 2 for further analysis.

In Stage 2, the environmental incident spectra (I_{env}) and leaf transmission spectra (I_1, I_2) were both inputs to the SDM for classifying plant stresses, including health status, nutrient deficiencies (N, P, K), and mite attacks.

First, two points of the spectral transmittance ($T_{s(1)}, T_{s(2)}$) were calculated as,

$$T_{s(i),(i=1,2)} = I_i / I_{env}.$$

After normalizing of $T_{s(1)}$ and $T_{s(2)}$, two sets of normalized spectral transmittance $\{\bar{T}_{s1}, \bar{T}_{s2}\}$ were contacted to form an integration array ($\bar{T}_{input}$). Then, the $\bar{T}_{input}$ was input into the SDM for diagnostic results output.

The pseudocode for the algorithms of the ML-powered diagnostic framework is as follows.

Algorithm 1 THD

Input: real-time input $\boldsymbol{T_{env}}$, $\boldsymbol{T_{leaf}}$, $\boldsymbol{H_{env}}$, $\boldsymbol{H_{leaf}}$ on every test day
Output: state of heat, drought, and senescence
Initialize: flag ← 0
ΔH_{max} ← max$\{\boldsymbol{H_{leaf} - H_{env}}\}$ *// calculate the maximum humidity difference in one day*
if T_{env} | T_{leaf} >= 35 ℃ **then** *// T_{env}* or *T_{leaf} above the threshold*
    return Heat
else if ΔH_{max} < 10% RH and flag = 0 **then** *// ΔH_{max} below the threshold*
    flag ← 1
    return Drought
else if ΔH_{max} < 10% RH and flag = 1 **then** *// ΔH_{max} still below the threshold on the other day*
    return Senescence
else
    flag ← 0
    go to Algorithm 2
end if

Algorithm 2 SDM

Input: real-time spectra data: $\boldsymbol{I_{env}}$, $\boldsymbol{I_1}$, $\boldsymbol{I_2}$
Output: state of health, nutrient deficiency (N, P, K), and mite attacks
$\boldsymbol{T_{s(i),(i=1,2)}} \leftarrow \boldsymbol{I_i / I_{env}}$ *// spectral transmittance*
$\overline{\boldsymbol{T}}_{\boldsymbol{si},(\boldsymbol{i=1,2})} \leftarrow \frac{S(m)}{\sum_{t=0}^{8} S(t)}$, $m \in [415, \ldots, 680]$ *// normalize of spectral transmittance*
$\overline{\boldsymbol{T}}_{\boldsymbol{input}} \leftarrow \{\overline{\boldsymbol{T}}_{\boldsymbol{s1}}, \overline{\boldsymbol{T}}_{\boldsymbol{s2}}\}$ *// contact two normalized spectral transmittances*
Load **SDM** *// load the trained ML model of SDM*
Predictions ← **SDM**.Predict($\overline{\boldsymbol{T}}_{\boldsymbol{input}}$)
return Predictions

Note S3. The classification mechanism of SDM

In general, the ML classification models can provide prediction probability for each class by assessing the likelihood of input spectral data belonging to each class. The classification probability is generally represented as $\boldsymbol{P(k \mid x)}$, denoting the probability that the input vector $\boldsymbol{x}$ belongs to class $\boldsymbol{k}$. Moreover, the form of $\boldsymbol{P(k \mid x)}$ varies depending on the classification model.

The SDM was established by ensemble learning strategy(*71*), which integrates seven base ML classification estimators to fully exploit the ability of these base estimators, including Logistic Regression (LR), Extra Trees (ET), AdaBoost, Support Vector Classifier (SVC), Random Forest (RF), Gradient Boost (GB), and Decision Tree (DT). Each of these models has a predefined probability function, as summarized in **table S5**.

The classification process of processing new spectral data is illustrated in **fig. S19**, which contains the following steps:

(1) Individual prediction probability generation.

When new spectral data is input into the SDM, each base estimator generates their classification prediction probability in five classes, represented as:

$$\boldsymbol{P_n} = \begin{bmatrix} P_n(k_1 \mid x) \\ P_n(k_2 \mid x) \\ P_n(k_3 \mid x) \\ P_n(k_4 \mid x) \\ P_n(k_5 \mid x) \end{bmatrix},$$

where $\boldsymbol{P_n}$ is a 5-dimensional column vector containing the predicted probabilities from base estimator n, and $P_n(k_i \mid x)$ represent the likelihood that the input vector x belongs to class k_i.

(2) Soft voting for weighted aggregation.

These individual probabilities are weighted and aggregated using a soft voting strategy to generate the final prediction probability. Therefore, the aggregated output probability for class k_i is given by:

$$P_{output}(k_i \mid x) = \frac{\sum_{n=1}^{7} w_n \cdot P_n(k_i|x)}{\sum_{n=1}^{7} w_n},$$

where $P_{output}(k_i \mid x)$ is the aggregated probability that the ensemble assigns input x to the class k_i, w_n is the weight assigned to classifier n, indicating its contribution to the ensemble prediction. Therefore, this formula calculates a weighted average of the probabilities for class k_i across all classifiers, ensuring that classifiers with higher weights contribute more to the final prediction. Also, the weights of different classifiers can be optimized to obtain a high accuracy.

(3) Final diagnostic result output.

Finally, the diagnostic result is determined by selecting the class with the maximum probability among all predicted classes, which is defined as follows,

$$\hat{k} = \underset{k_i}{\operatorname{argmax}} P_{output}(k_i \mid x),$$

where $\hat{k}$ is the final diagnostic class result for new input spectral data.

Therefore, the ML-diagnostic framework can both output the diagnosis probability of each class and the final classification class.

Note S4. Performance evaluation of the SDM

The classification performance of SDM was conducted by compared with other common deep learning (DL) approaches, such as CNNs, LSTMs, and Bi-LSTMs. The details of evaluation metrics (including average accuracy, F1-score, 10-fold cross-validation, and training time) are summarized in **table S6**. Based on the results, the advantages of SDM over other DL approaches are as follows.

1. Robustness and generalization: The SDM demonstrates greater robustness in diagnosis, whereas deep learning models tend to exhibit overfitting or underfitting. The reason is that SDM has significantly fewer parameters, making it more suitable for generalization with a small training dataset (2742 spectral sequences of 500 leaves) than DL methods.

2. Suitability for tabular spectral data: As a tree-based model, the SDM is well-suited for classifying the tabular spectral data, whereas deep learning models may struggle to efficiently capture these interactions.

3. Lower training time: The SDM requires significantly less training time compared to deep learning methods, enhancing its practicality and applicability.

Note S5. Calculation of leaf pigment contents

As the leaf pigments (including chlorophyll, carotenoids, and anthocyanins) possess specific spectral features, their contents can be calculated from the spectral reflectance(*46*), as shown following,

$$\text{chlorophyll} = \frac{R_{800}-R_{680}}{R_{800}+R_{680}},$$

$$\text{carotenoid/chlorophyll} = \frac{R_{531}-R_{570}}{R_{531}+R_{570}},$$

$$\text{anthocyanin} = \frac{\sum_{i=600}^{699} R_i}{\sum_{i=500}^{599} R_i},$$

where R_x refers to spectral transmittance at wavelength x nm. Therefore, according to the reflectance results in **fig. S46**, pigment contents of leaves in different health statuses can be calculated.

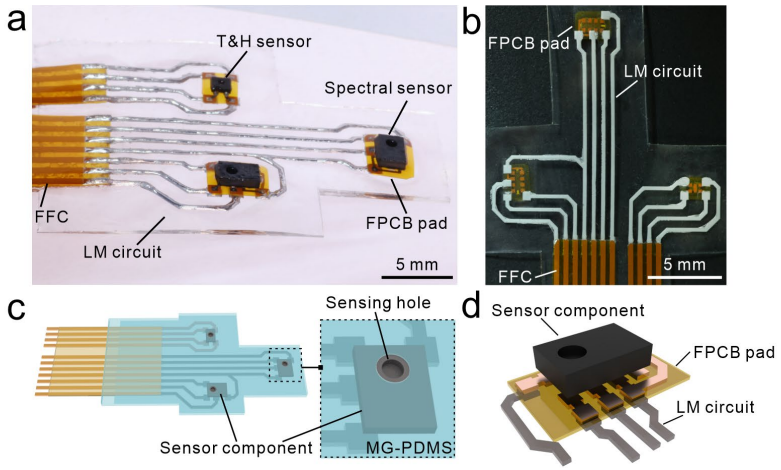

Fig. S1. Details of the soft sensor patch: (**a**) Front view, (**b**) Backside view, (**c**) Schematic illustrating the exposed sensing hole of the sensor component, which is not covered by the MG-PDMS substrate, and (**d**) Schematic depicting the FPCB board extending sensor component pins for easier alignment with the LM circuit. [Photo credit: Q.J., HUST]

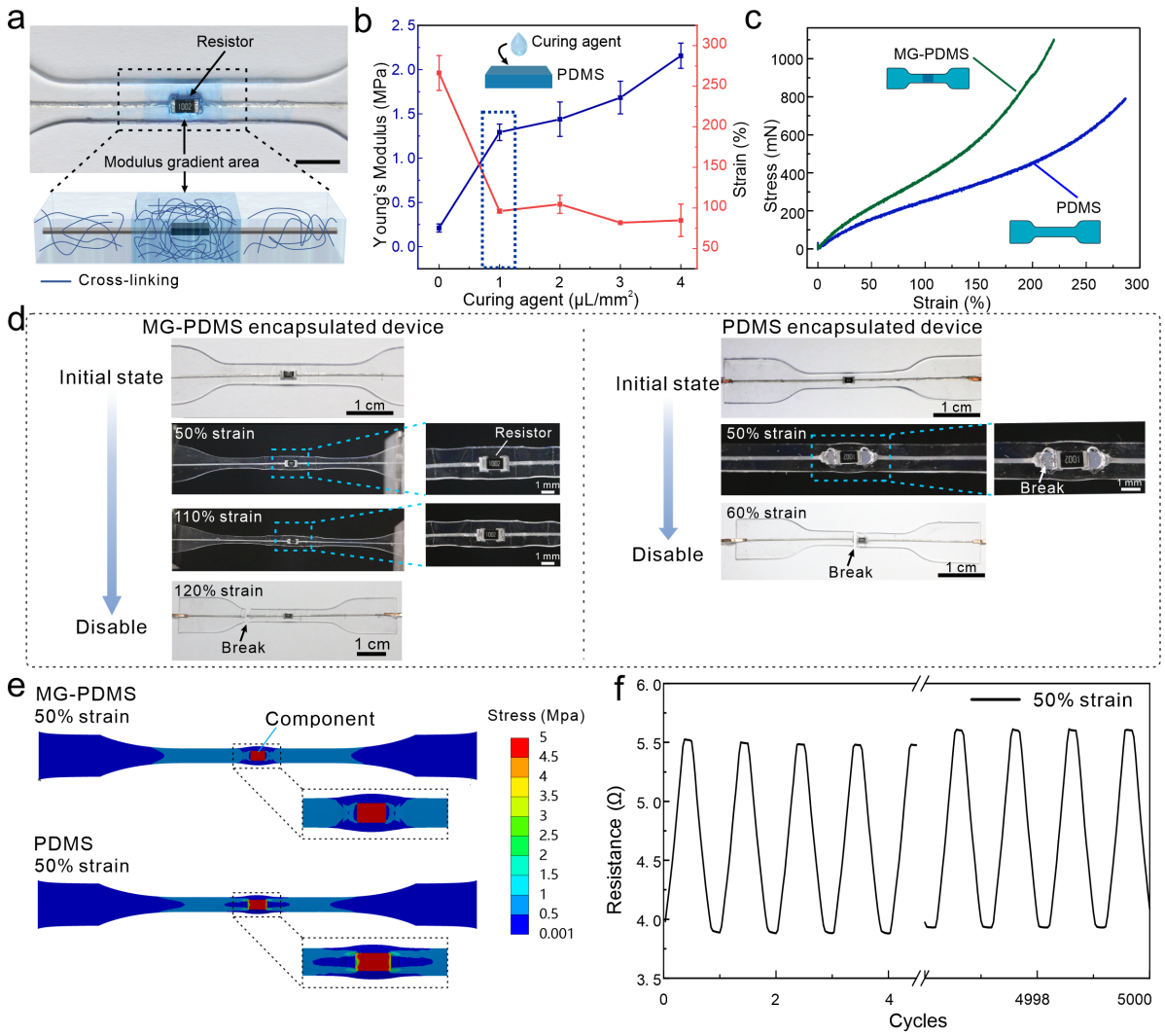

Fig. S2. Characteristics of the MG-PDMS substrate. (**a**) Photo and schematic of the components encapsulated in the MG-PDMS substrate. (**b**) Young's modulus and strain response to different curing agents rations in PDMS substrate. (**c**) Stress-strain curves of MG-PDMS and PDMS substrate. (**d**) Comparison of MG-PDMS and PDMS substrates encapsulated with resistors under strain. The MG-PDMS substrate withstands up to 110% strain, while the PDMS substrate fails at 50% strain. (**e**) Stress distribution simulation results for MG-PDMS and PDMS both under 50% strains. (**f**) Resistance measurement of a resistor integrated into the MG-PDMS structure during a 5000-cycle mechanical loading test at 50% strain and 0.5 Hz. The device's resistance increased slightly from 3.94 ohm (Ω) to 4.08 Ω after 5000 cycles (details in **fig. S47**).

Experimental details: Tensile tests of the MG-PDMS and PDMS specimens were conducted with a universal tensile test instrument (1 kN, 5944, Instron) at a 100 mm/min strain rate at room temperature. The cyclic mechanical loading test was conducted using a dynamic mechanical test system (E1000, Instron) through a program (50% strain, 0.5 Hz, 0.5 mm s^{-1}) for 5000 times cycling. The resistance change of specimens was measured by a digital multimeter (34, 461A, KeySight Technologies) at a 10 Hz measurement frequency. The simulation was conducted using COMSOL 5.6a.

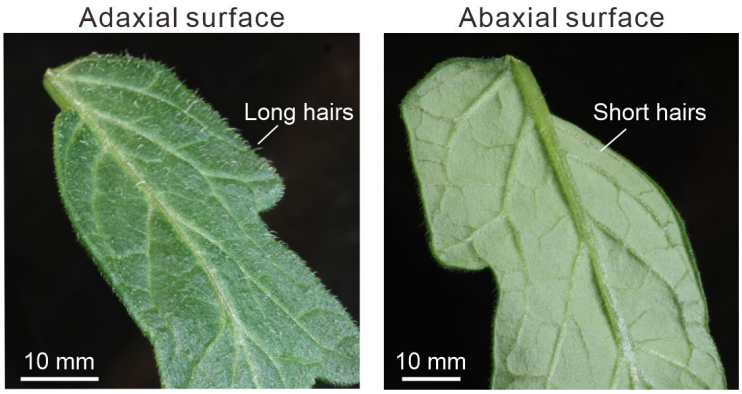

Fig. S3. Photos of the hairs on the adaxial and abaxial surface of a tomato leaf. Long hairs primarily grow on the adaxial surface of tomato leaves, while the abaxial side—where the soft sensor patch is attached—has only soft, short hairs. [Photo credit: Q.J., HUST]

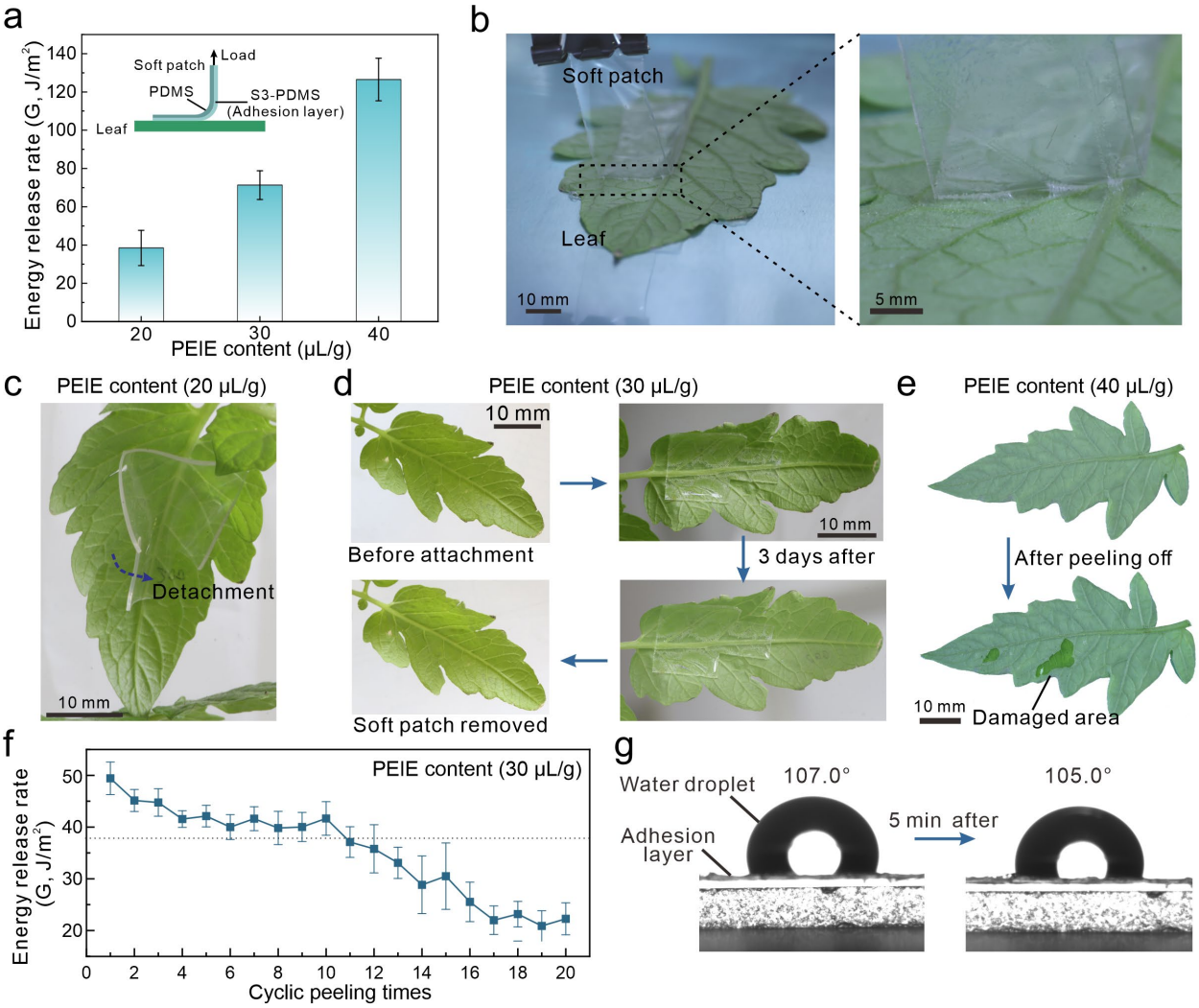

Fig. S4. Adhesion characteristics of the adhesion layer. (**a**) The energy release rate of adhesion layers (S3-PDMS) on the abaxial leaf surface in response to varying dosages of PEIE. (**b**) Photos showing the soft patch peeling from the abaxial leaf surface. (**c-e**) Photos of the adhesion characteristics of the S3-PDMS with different PEIE contents: (**c**) The S3-PDMS with 20 μL/g of PEIE content shows insufficient adhesion, detaching easily from the leaf surface. (**d**) The S3-PDMS with 30 μL/g of PEIE content has sufficient adhesion force to adhere to the leaf surface for 3 days, without causing damage to the leaf after the soft patch is removed. (**e**) The S3-PDMS with 40 μL/g of PEIE content has excessive adhesion force that can generate damage to the leaf surface after being peeled off. (**f**) Energy release rate variation of the adhesion layer with 30 μL/g PEIE content under cyclic peeling. After 10 peeling cycles, the adhesion layer exhibits a significant decline in energy release rate, similar to that of the 20 μL/g PEIE content, making it easier to detach from the leaf. This result indicates that the adhesion layer can maintain repeated adhesion for approximately 10 cycles. (**g**) Photos of the static angle of water droplet on the adhesion layer before and after 5 minutes, indicating its hydrophobic and water-resistant properties.

Experimental details: Energy release rate measurement was based on an international standard test method for 90° peeling resistance of energy release rate (ASTM D 6862-2004) and a test

method for peeling strength of pressure-sensitive tape (GB/T 2792-1981). The adhesion force was conducted with a homemade measurement setup of a force transducer at a peeling speed of 100 mm s^{-1}. The soft patches were cut into a rectangle shape (length: 60 mm, width: 10 mm, and thickness: 200 μm). After the soft patch was laminated on the abaxial leaf surface, a roller was employed to ensure the attachment tightly and evenly before the peeling test. The energy release rate (G) is defined as $G = F/w$, where the F refers to adhesion force and the w refers to the width of samples.

Referring to our previous work(*72*), the S3-PDMS layer was fabricated by adding ethanol-diluted polyethyleneimine ethoxylated (PEIE) solution (volume fraction: 5 vol%) into a PDMS mixture (20:1 ratio of curing agent to silicone base). In the experiment, the S3-PDMS was prepared with the PEIE variation of 200, 300, and 400 μL in 10g of the PDMS mixture. Then, the S3-PDMS coating was applied to the soft patch surface and cured at 75°C for two hours.

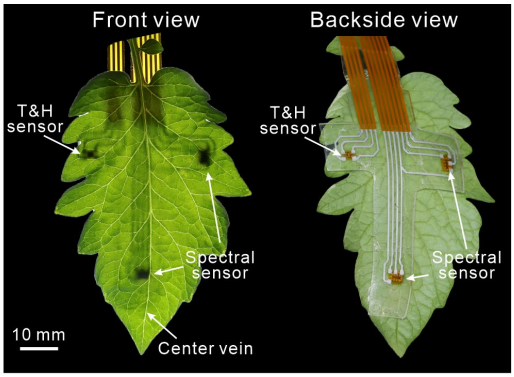

Fig. S5. Photos of the spatial distribution of sensors at different views after attachment to the leaf.

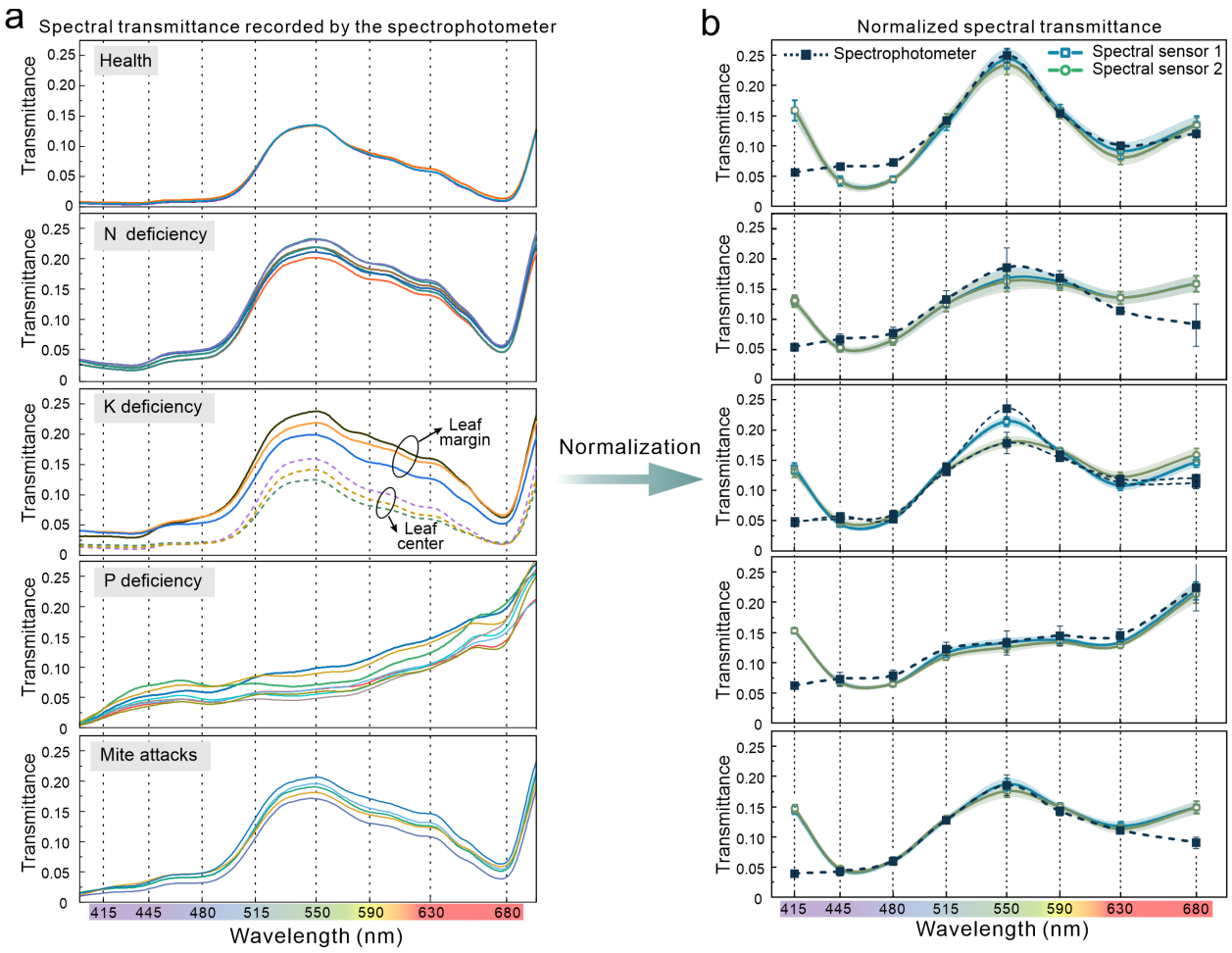

Fig. S6. Comparison of spectral transmittance collected by the spectrophotometer and spectral sensor. (**a**) Spectral transmittance of leaves in different health statuses, recorded by the spectrophotometer. Transmittance values at specific wavelengths (415, 445, 480, 515, 550, 590, 630, and 680 nm) were selected and normalized for further comparison. (**b**) Comparison of normalized spectral transmittance for various leaf types, measured with the spectrophotometer (dashed lines) and the spectral sensor component (solid lines).

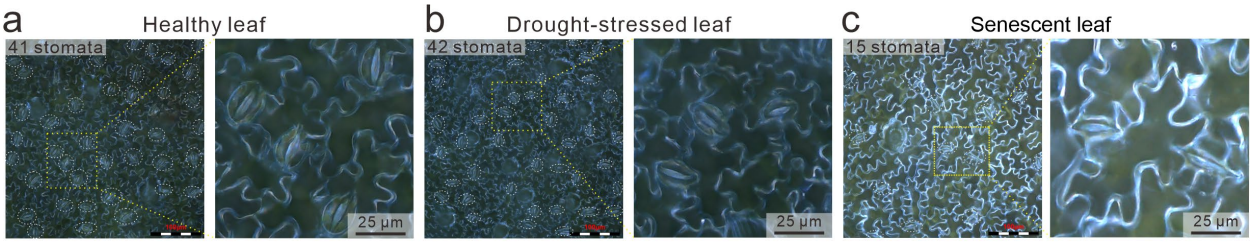

Fig. S7. Photos of stomatal status on leaves under healthy, drought-stressed, and senescent conditions. Stomata are marked by dash circles, and the number of stomata within each image is labeled.

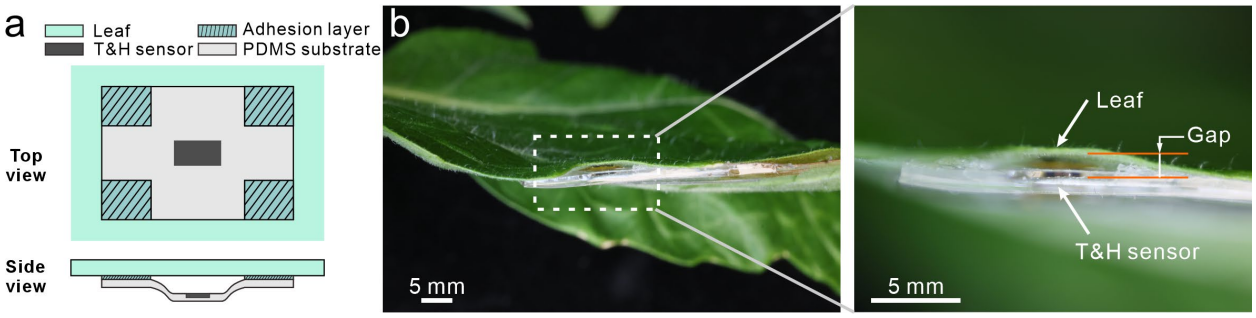

Fig. S8. Design of the gap between the T&H sensor and leaf to prevent water vapor accumulation. (**a**) Illustration of the T&H sensor attached to a leaf, showing the adhesion layer surrounding the sensor (top view) and creating a gap between the leaf and sensor (side view). (**b**) Photos of the T&H sensor attached to the abaxial leaf surface.

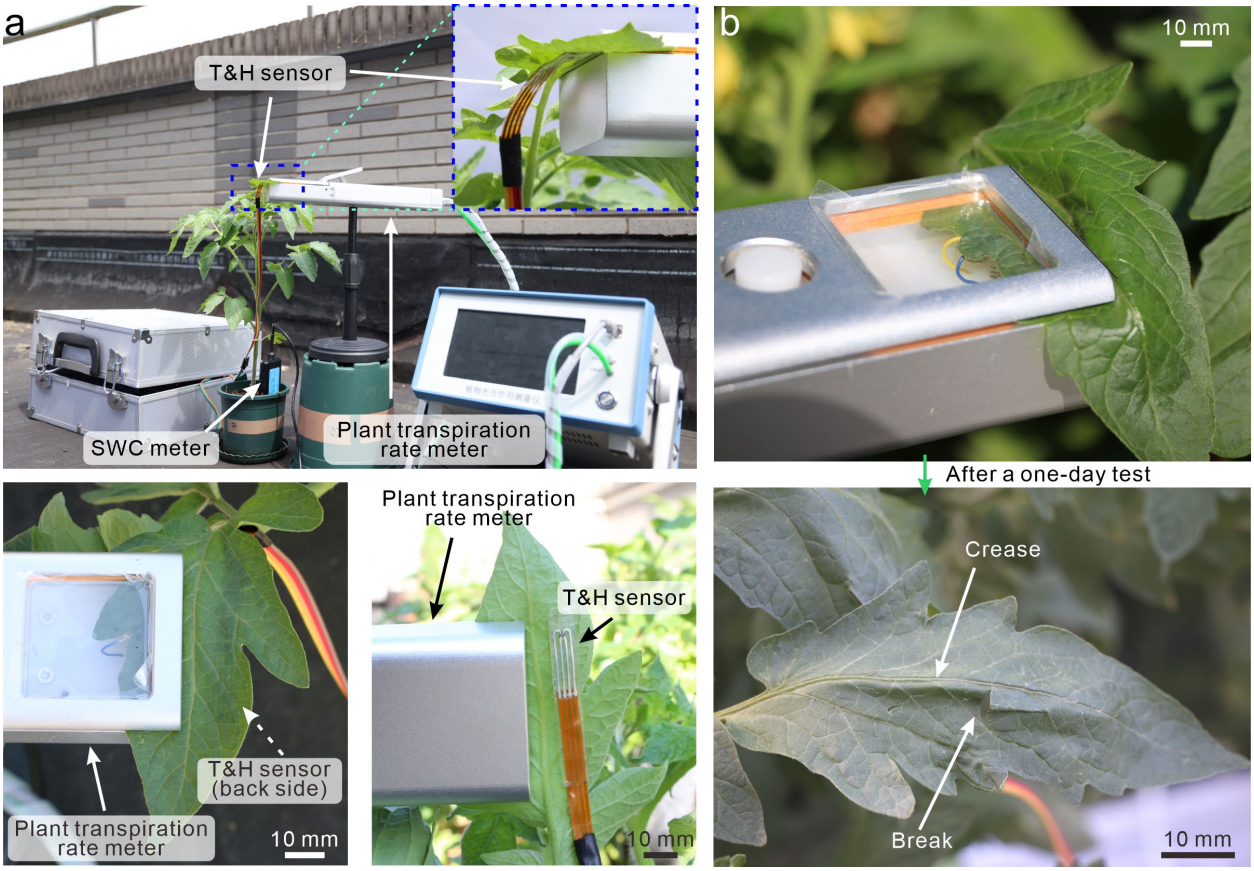

Fig. S9. Transpiration rate measurement of tomato leaves. (**a**) Photo of the outdoor transpiration rate measurement using a soft T&H sensor and a commercial plant transpiration rate meter. A soil water content (SWC) meter probe is inserted into the soil to monitor its water content. (**b**) Photos showing the crease and break area on the leaf caused by the commercial plant transpiration rate meter after a one-day test. [Photo credit: Q.J., HUST]

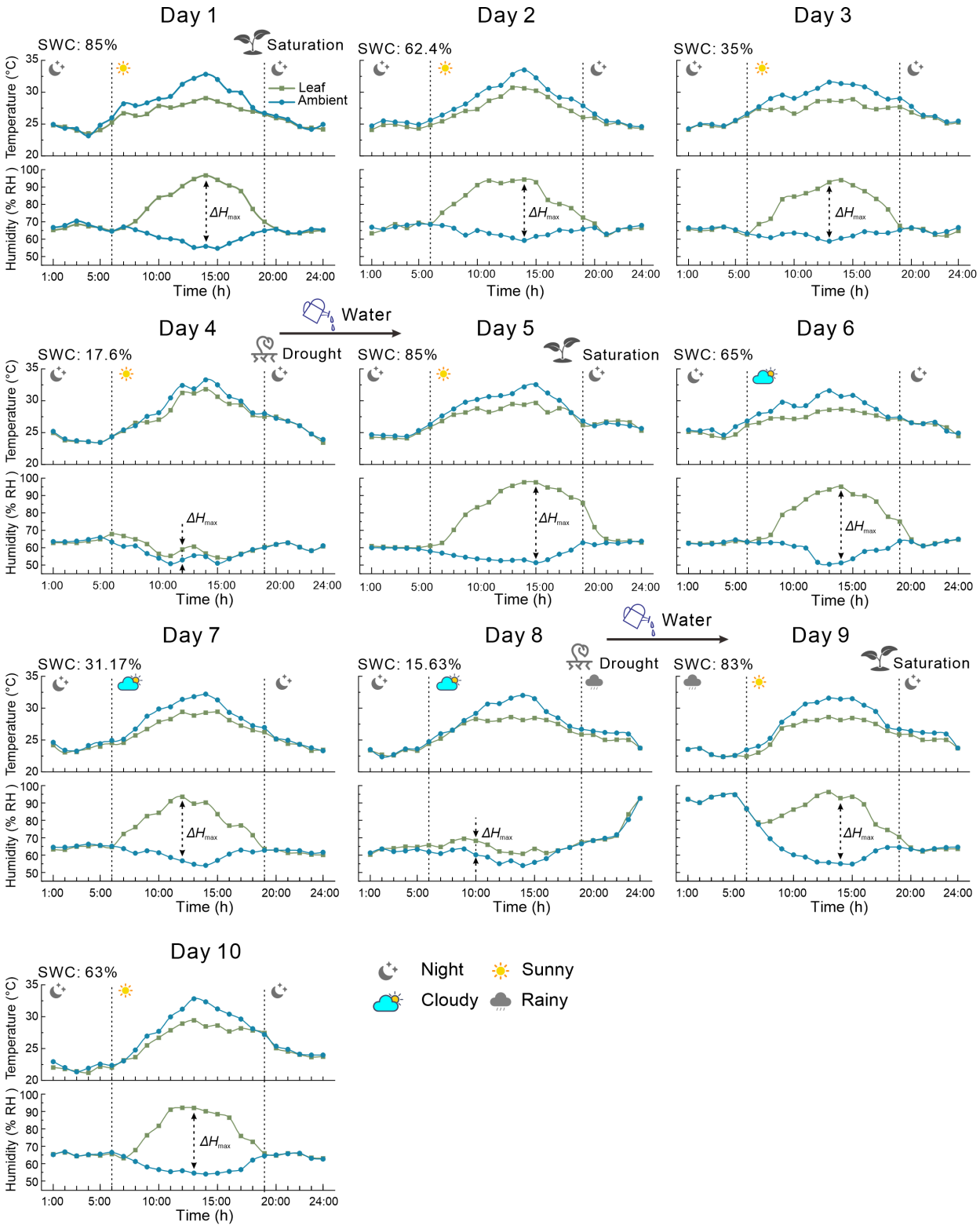

Fig. S10. Continuous 10-day outdoor measurement of T&H for both leaf and surrounding environment. The outdoor weather conditions vary by weather (sunny, rainy, cloudy) and time (day/night). When the plant is under drought stress, the ΔH_{max} shows lower than 10 %RH. SWC: Soil water content.

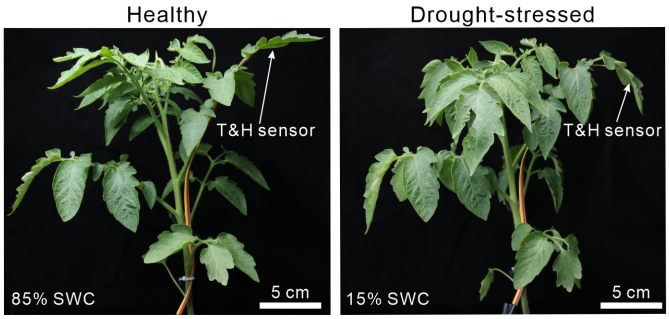

Fig. S11. Photos showing the tomato plant in healthy and drought-stressed conditions. Despite branches wilting under drought stress, the T&H sensor remains conformally attached to the tested leaf. SWC: Soil water content. [Photo credit: Q.J., HUST]

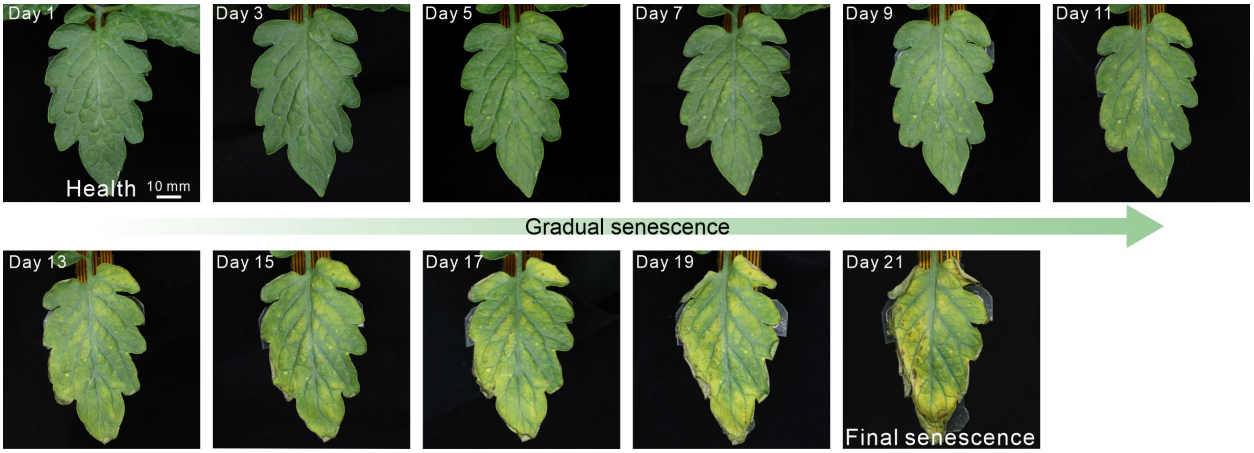

Fig. S12. Sequential photos depicting the gradual senescence of a tomato leaf.

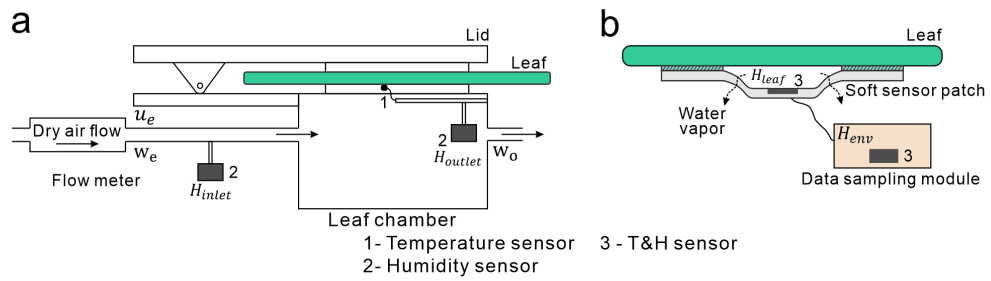

Fig. S13. Diagram showing the measuring method of plant transpiration rate (*Tr*). (**a**) Schematic of a commercial transpiration meter for measurement of *Tr* measurement. u_e and u_o denoted the air flow rate (mol s^{-1}) entering and exiting the leaf chamber, respectively, while w_e and w_o represent the mole fractions of water vapor at the inlet and outlet. The inlet and outlet humidity (H_{inlet} and H_{outlet}) are monitored using humidity sensors. (**b**) Schematic showing soft sensor patch that collects T&H data from the leaf and surrounding environment during transpiration. The leaf-surface surrounding humidity (H_{leaf}) and ambient humidity (H_{env}) are collected by the T&H sensors.

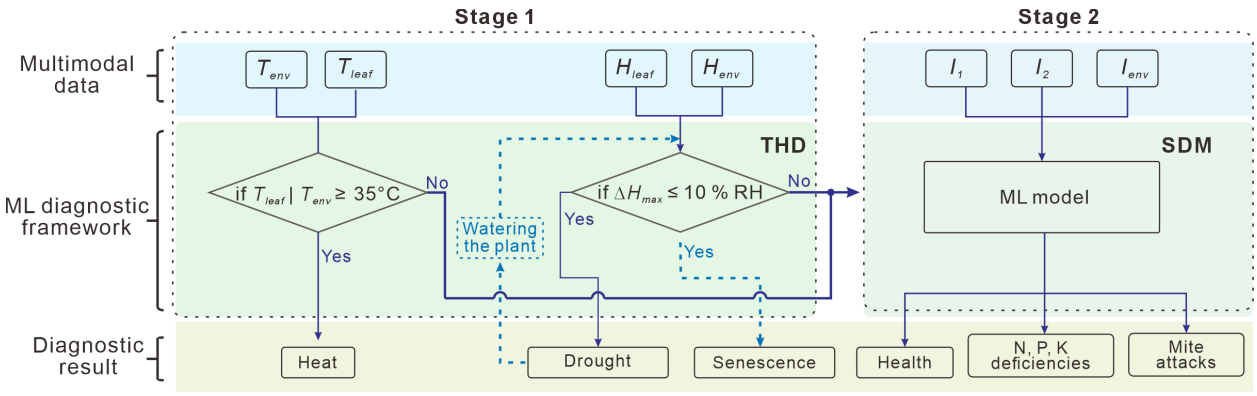

Fig. S14. Workflow of the ML-powered diagnostic framework. The framework consists of two modules: THD and SDM. **In Stage 1**, the THD analyzes outliers in T&H data caused by plant stresses like heat, drought, and senescence. Until the T&H data is normal, the framework proceeds to Stage 2. **In Stage 2**, the spectral data from the leaf and environment are input into the SDM to classify plant statuses, including health, nutrient deficiencies (N, P, K), and mite attacks.

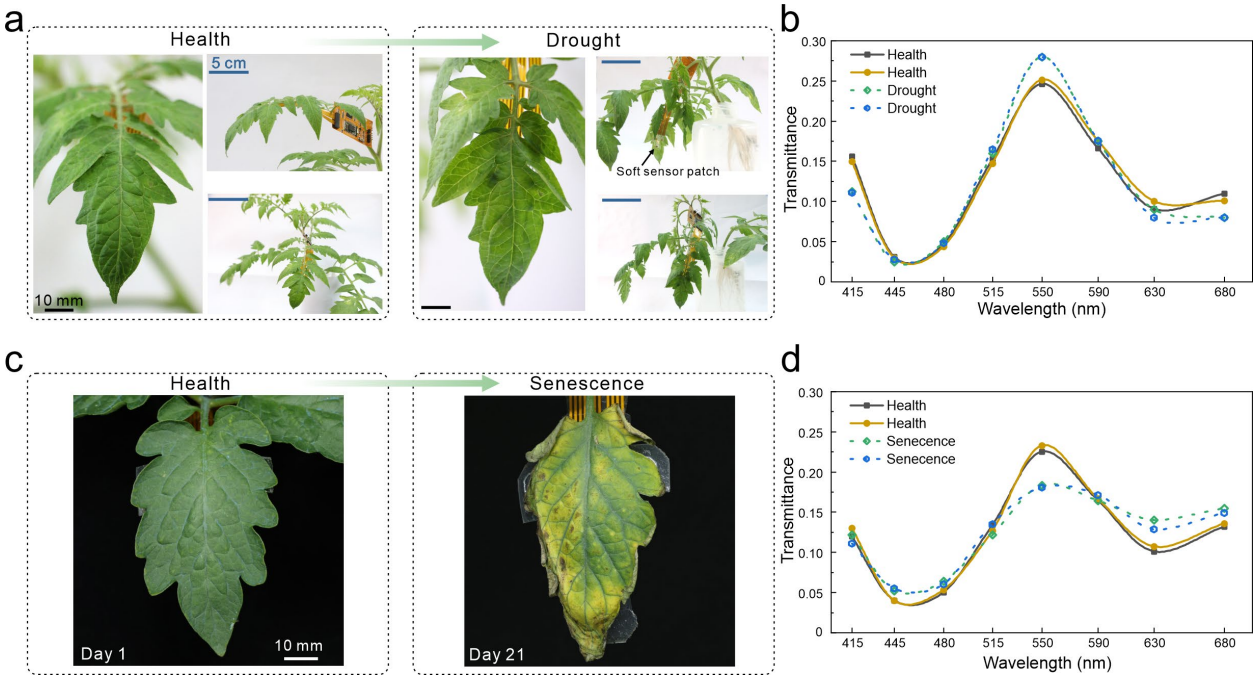

Fig. S15. Leaf spectral data affected by drought and senescent stress. (**a**) Photos showing the morphology of leaves and branches transitioning from healthy to drought conditions. (**b**) Spectral transmittance of the leaf under healthy and drought conditions. (**c**) Photos showing the progression of leaf symptoms from healthy to senescent states. (**d**) Spectral transmittance of the leaf under healthy and senescent conditions, showing significant differences between the two states. [Photo credit: Q.J., HUST]

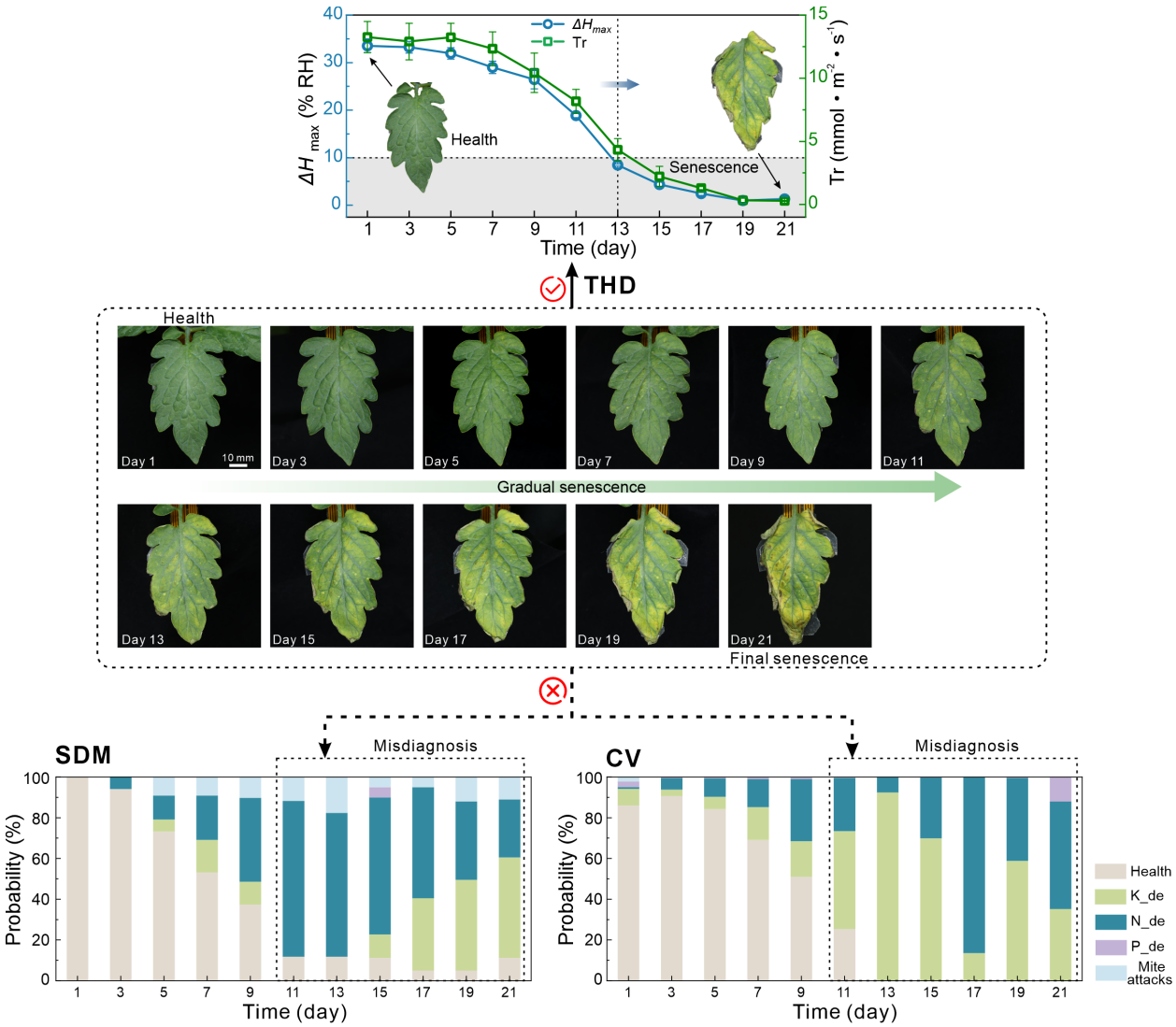

Fig. S16. Diagnostic results of leaf senescence via THD, SDM, and CV method. The results show that the THD successfully diagnosed the leaf senescence after the 13th day, as the ΔH_{max} gradually drops below 10% RH. In contrast, the SDM and CV methods misdiagnosed the stress as N or K deficiency due to interference from leaf senescence.

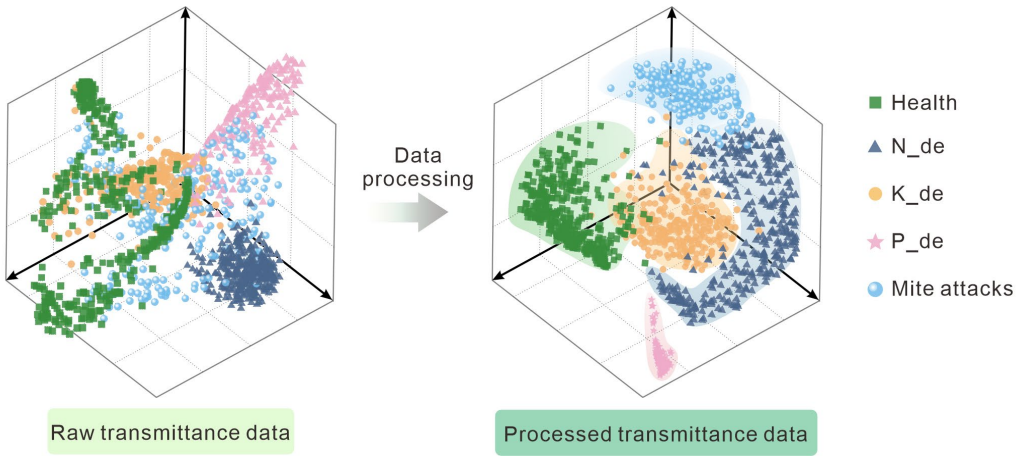

Fig. S17. kPCA results showing 3D spatial distribution of raw and processed spectral transmittance data. The projected data of raw spectral transmittance fails to be distinguished among different labels. In contrast, the processed data can be differentiated by the kPCA, illustrating the effectiveness of data processing. Abbreviations: N deficiency (N_de), K deficiency (K_de), P deficiency (P_de).

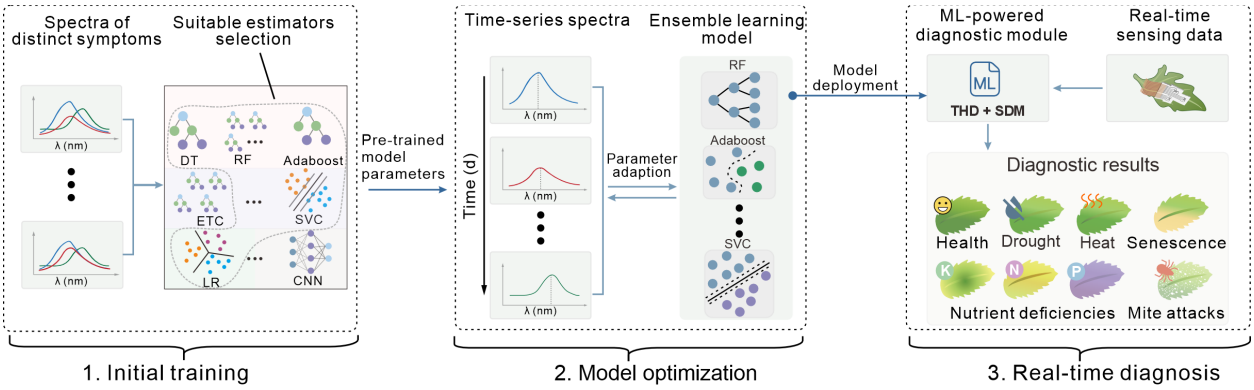

Fig. S18. Schematic of the SDM development process.

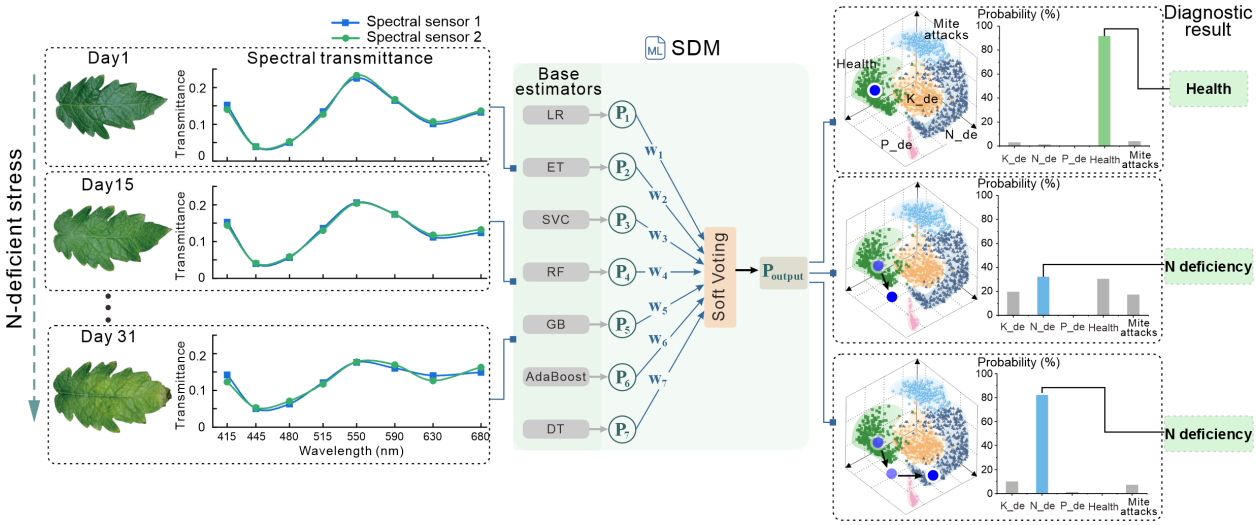

Fig. S19. Schematic of the ML-powered diagnostic framework for long-term diagnosing during gradual stress progression. For instance, under the N-deficient stress, the leaf's spectral data and visual symptoms gradually change over time. The spectral data's projected position (purple circle) in the kPCA space also shifts progressively from the healthy (green region) to the N-deficient (cyan region) zone. The diagnostic result is determined by selecting the class with the highest probability among all predicted classes. The final prediction probability (P_{output}) is computed as a weighted sum of the classification prediction probabilities from individual estimators, where P_n and w_n represents the classification prediction probability and weight assigned to each estimator n, respectively.

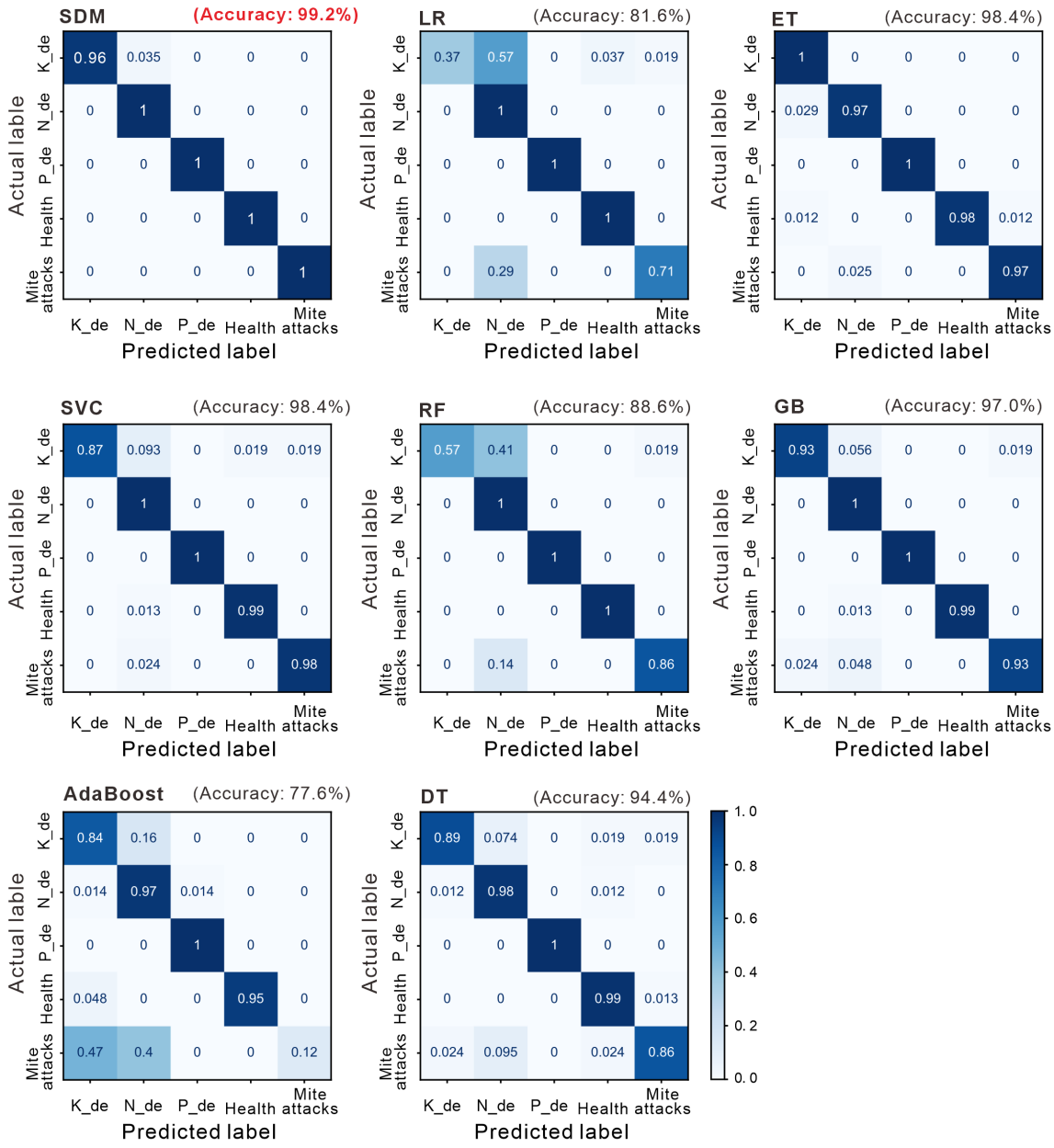

Fig. S20. Confusion matrix illustrating the performance of the SDM compared to its base estimators in recognizing plant stresses. Results show that the SDM possesses the highest prediction accuracy among other base estimators. Logistic Regression (LR), Extra Trees (ET), AdaBoost, Support Vector Classifier (SVC), Random Forest (RF), Gradient Boost (GB), and Decision Tree (DT).

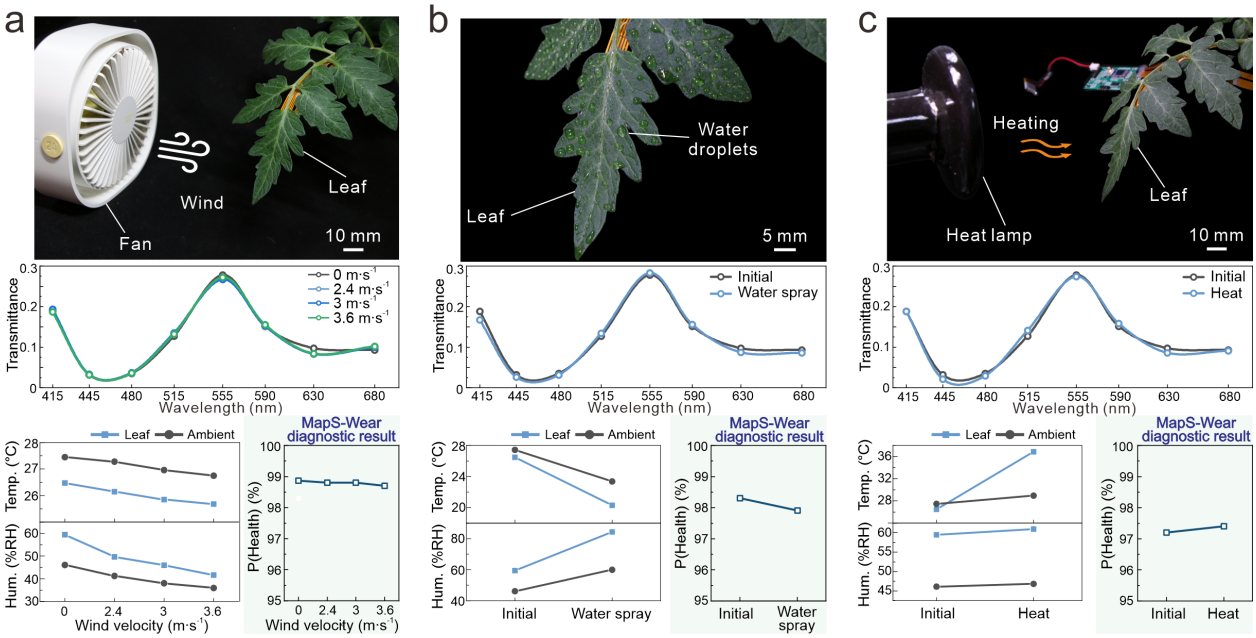

Fig. S21. Diagnosis stability of MapS-Wear under (a) wind exposure, (b) water spray, and (c) heat conditions, simulating outdoor environmental disturbances. Photos illustrate the tested leaf under each condition. Spectral transmittance and T&H data variations under these conditions are also provided. Despite these disturbances, the diagnostic probability of health, *P(Health)*, remains stable, indicating that MapS-Wear maintains reliable diagnostic performance. Abbreviations: Humidity (Hum.), Temperature (Temp.).

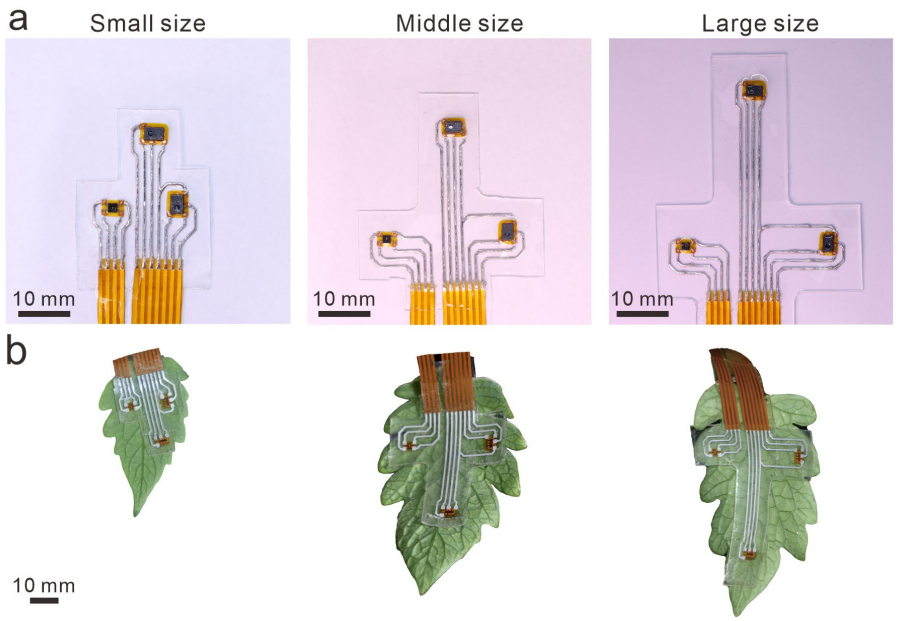

Fig. S22. Customizable soft sensor patch designed for various leaf sizes. (**a**) Photos showcasing soft sensor patches fabricated in multiple dimensions to accommodate different leaf sizes. (**b**) Images showing the attachment of these soft sensor patches to leaves of varying sizes.

Fig. S23. Photos of leaves under N-deficient stress and subsequent N replenishment. (**a-c**) Sequential photos showing symptom changes in the upper, middle, and lower leaves. (**d**) Photos showing the growth of the tomato plant from day 1 to 31. [Photo credit: Q.J. and X.Z., HUST]

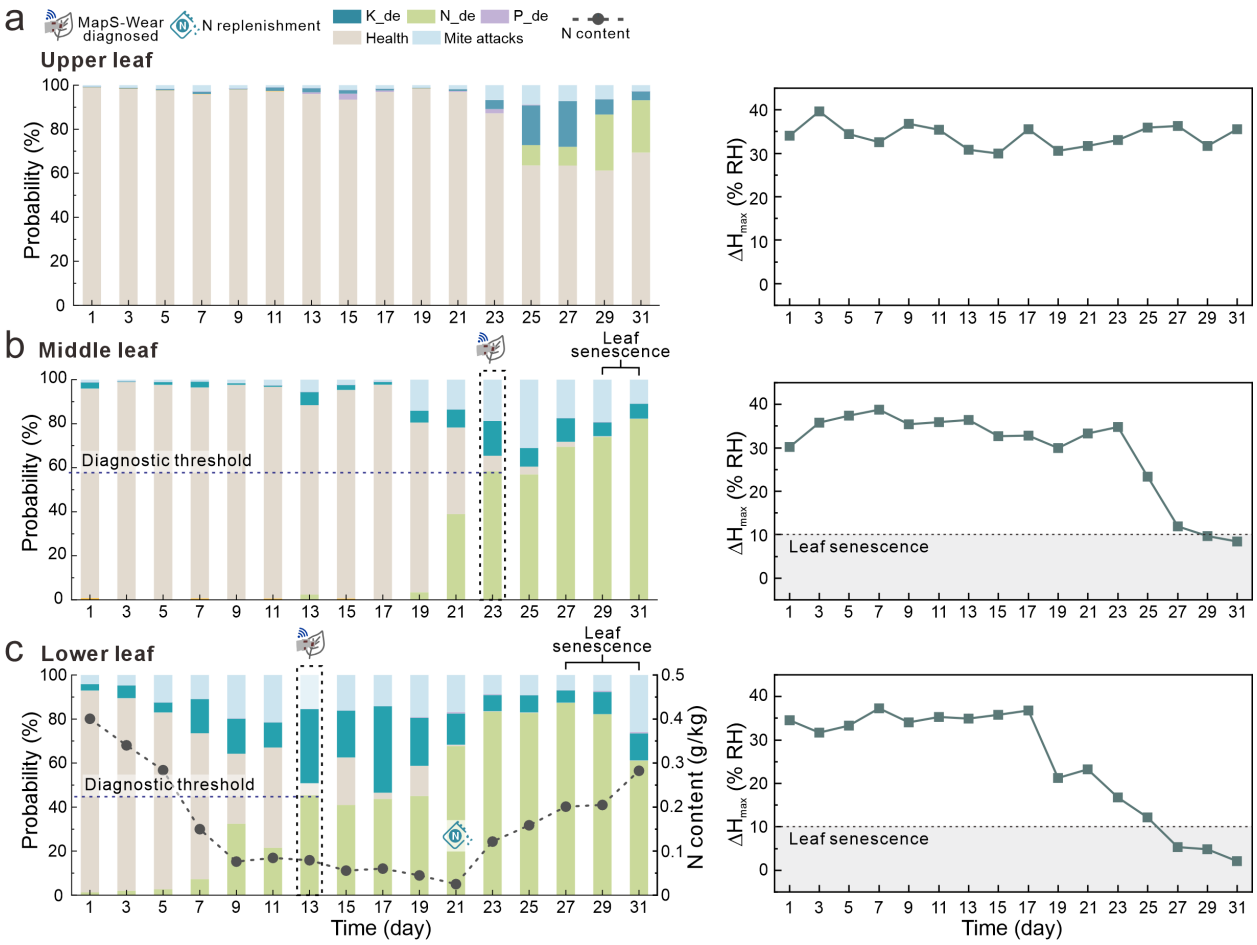

Fig. S24. Diagnostic results of different leaves under N-deficient stress using MapS-Wear. (**a-c**) Diagnostic probabilities of upper to lower leaf health status under the N-deficient stress and subsequent N replenishment, as diagnosed by MapS-Wear. The ΔH_{max} variations of different leaves were also recorded throughout the long-term experiment. The diagnostic threshold means that the *P(N)* reaches the maximum among all other classifications. When the ΔH_{max} falls below 10% RH, the system diagnoses the leaf as undergoing senescence.

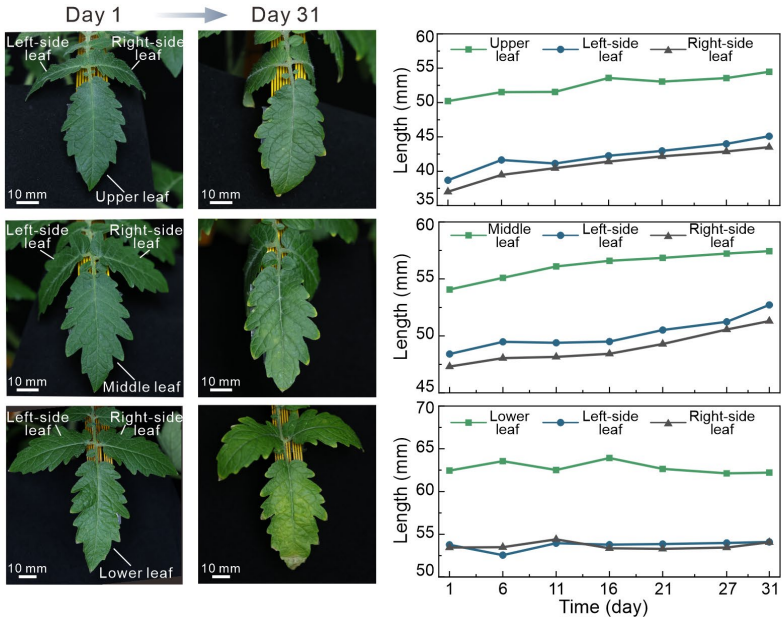

Fig. S25. Leaf length variation over 31 days under N-deficient stress, including lower to upper leaves and their corresponding left and right-side leaves.

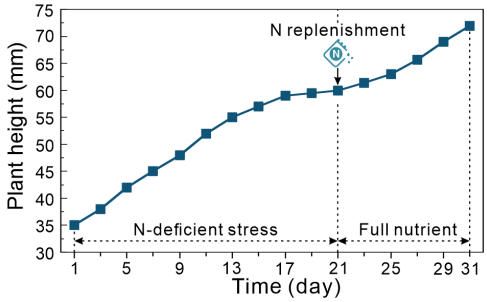

Fig. S26. Plant height variation during periods of N-deficient stress and subsequent nutrient replenishment.

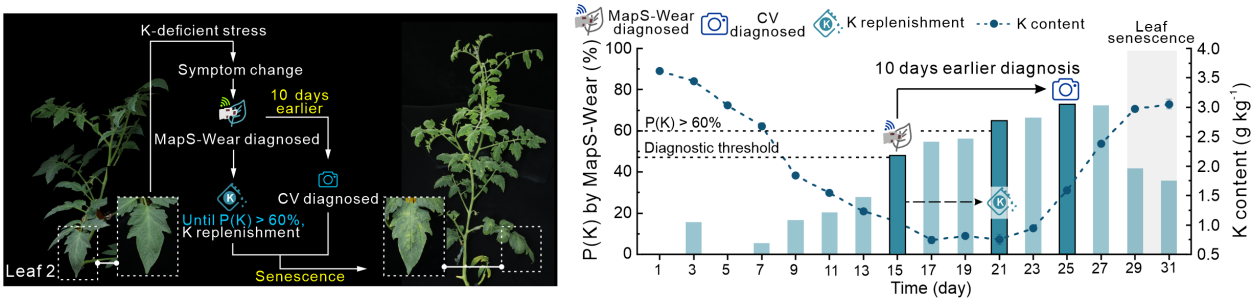

Fig. S27. Continuous diagnosis of Leaf 2 experienced K-deficient stress and subsequent K replenishment. Photos and flow diagrams outline the experiment process, while charts show variations in *P(K)* by MapS-Wear and overall plant K content.

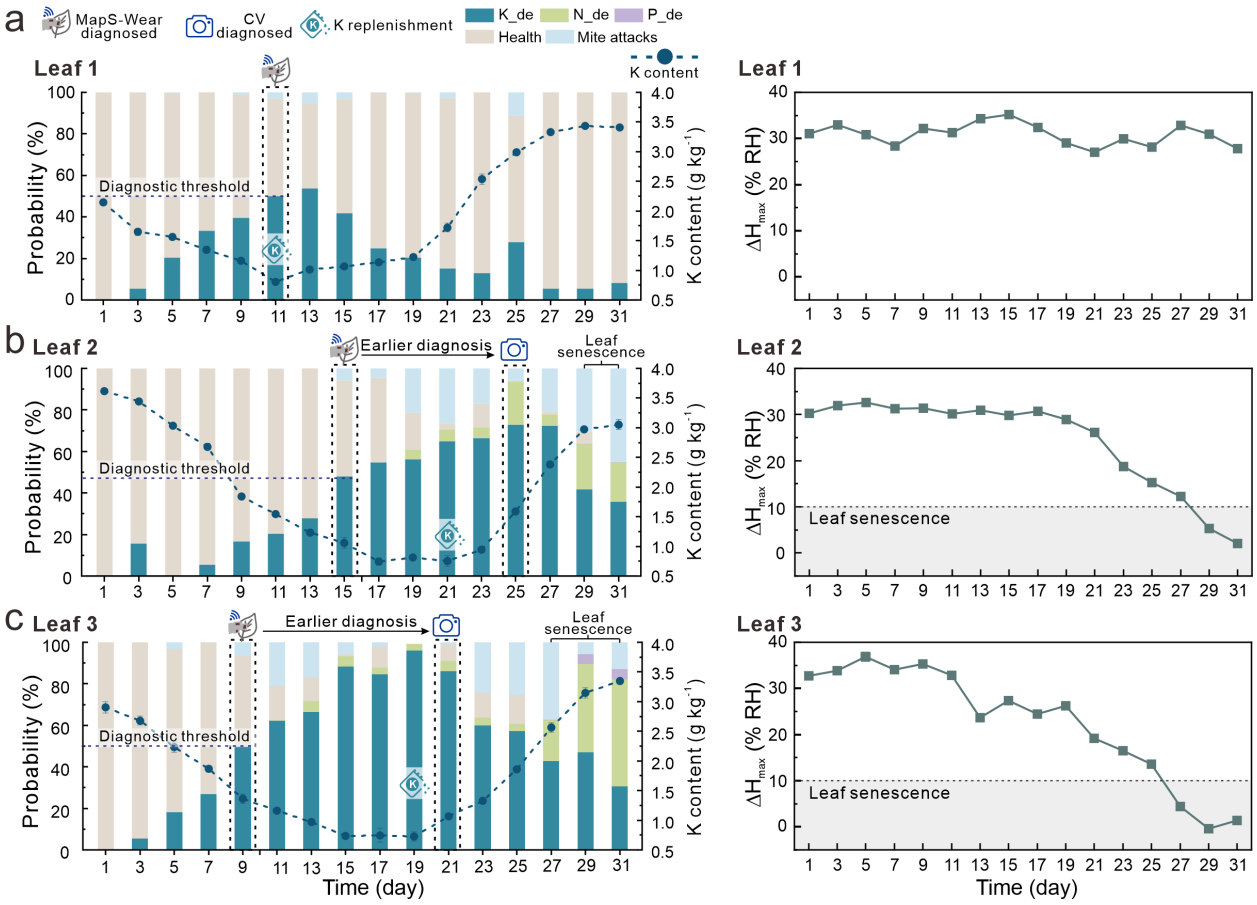

Fig. S28. Diagnostic results of leaves under K-deficient stress via MapS-Wear. (**a-c**) Diagnostic probabilities of Leaves 1 to 3 in different health statuses under K-deficient stress and subsequent K replenishment, as diagnosed by MapS-Wear. The variations in ΔH_{max} for different leaves are also recorded throughout the long-term experiment. The diagnostic threshold corresponds to where *P(K)* reaches its maximum among all other health status classifications. When the ΔH_{max} falls below 10% RH, the MapS-Wear diagnoses the leaf as undergoing senescence.

Fig. S29. Photos of tomato plant leaves under K-deficient stress and subsequent K replenishment. (**a–c**) Sequential photos showing symptom changes in Leaves 1–3. (**d**) Photos illustrating the growth phenotypes of tomato plants from day 1 to day 31. [Photo credit: Q.J. and X.Z., HUST]

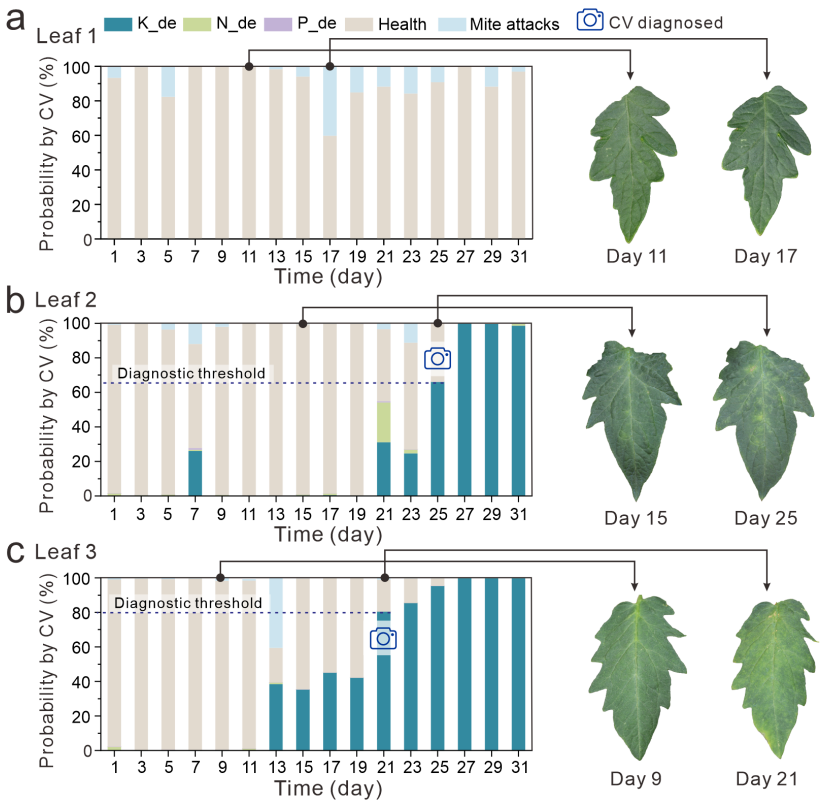

Fig. S30. Diagnostic results of Leaves 1 to 3 under K-deficient stress using the CV method. (**a-c**) Diagrams showing the diagnostic probabilities of different health statuses by CV method over 31 days: (**a**) For leaf1, symptom changes under K-deficient stress cannot be diagnosed by CV method throughout the entire period. (**b**) For leaf 2, the CV method fails to diagnose K deficiency on the 15th day (while MapS-Wear diagnoses it) but becomes diagnoseable on the 25th day. (**c**) For Leaf 3, the CV method cannot diagnose K deficiency on the 9th day (while MapS-Wear diagnoses it) but becomes diagnoseable on the 25th day.

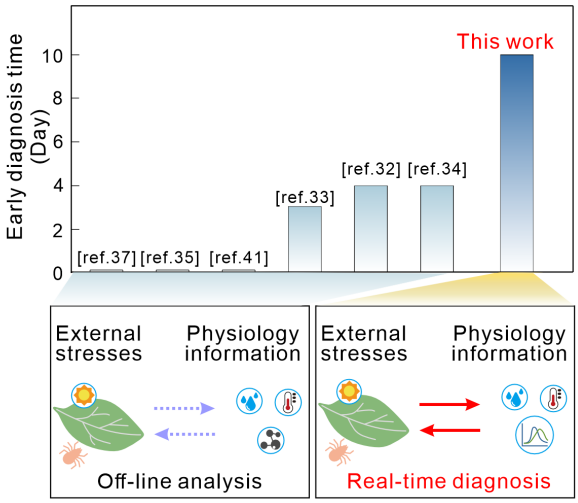

Fig. S31. Performance comparison of MapS-Wear and existing plant soft wearable sensors. Our MapS-Wear achieves the earliest detection of plant stresses (10 days) compared to other reference works. Unlike other systems that only detect physiological information resulting from stress, our MapS-Wear achieves real-time plant physiology detection and stress diagnosis.

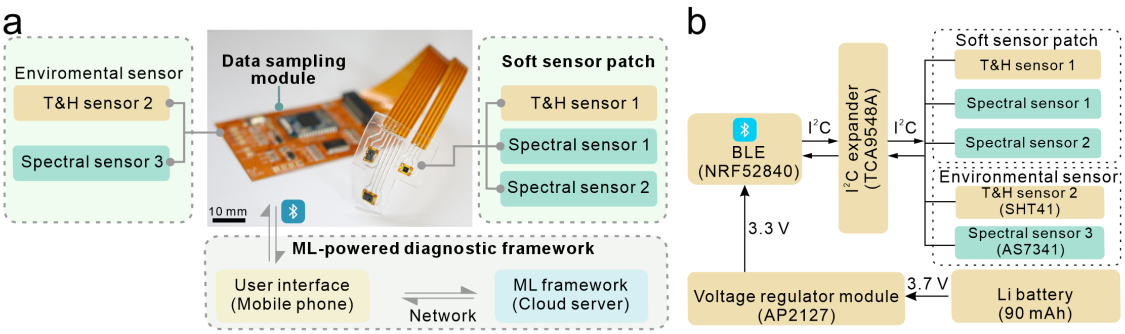

Fig. S32. Overall architecture design of the MapS-Wear. (**a**) Photo and system architecture schematic of the MapS-Wear. The soft sensor patch is connected to the FPCB via a soft cable for data transmission and power supply. (**b**) Schematic diagram illustrating the hardware architecture of the MapS-Wear. [Photo credit: Q.J., HUST]

Experimental details: The FPCB integrates a Bluetooth Low-Energy (BLE) microcontroller (NRF52840, Nordic), an Inter-Integrated Circuit (I^2C) expander (TCA9548A, Texas Instruments), a voltage regulator module (AP2127, Diodes Incorporated), a small Li-ion battery (35×20×14 mm, 90 mAh), and passive components such as resistors, capacitors, and inductors. The BLE communicates with the sensors through the I^2C expander and processes the data for transmission to mobile phones via Bluetooth at 5-second intervals.

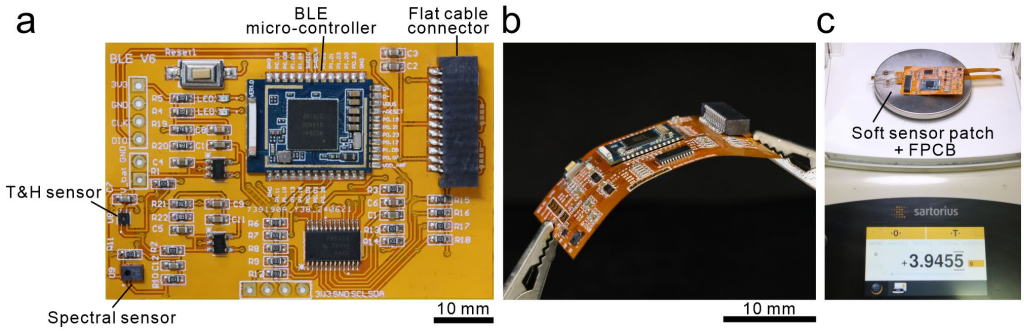

Fig. S33. Photos of the FPCB-based data sampling module. (**a**) Top view of the FPCB. (**b**) Side view of the FPCB under bending, showing its good flexibility. The FPCB used polyimide (PI) as the substrate with 139 μm thickness, showing its high flexibility. (**c**) Photos showing the mass measurement of the soft sensor patch and the FPCB.

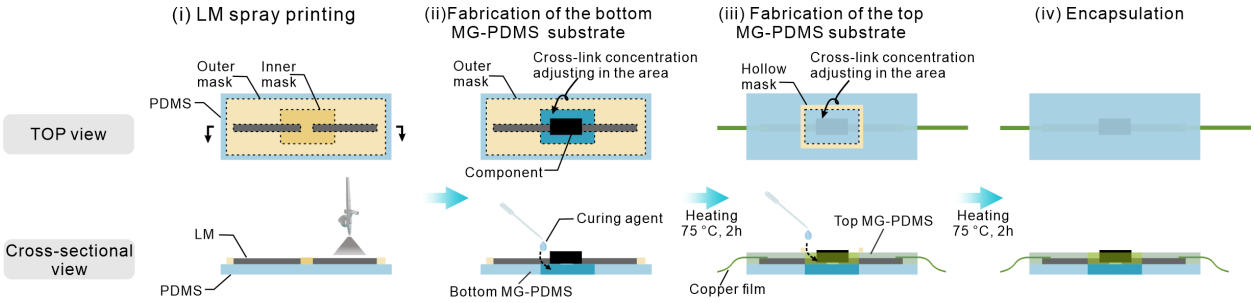

Fig. S34. Fabrication process of the MG-PDMS structure. The fabrication process of the MG-PDMS structure integrated with components can be summarized into four main steps: (**i**) The PDMS (Sylgard 184, Dow Corning Corporation) was prepared by mixing the silicone base and curing agent at a 20:1 weight ratio. After vacuuming to remove air bubbles, a thin PDMS substrate (250 μm thickness) was coated on an aluminum plate using a thin-film scraper. The substrate was then semi-cured at 70°C for 20 minutes in an oven. A polyethylene terephthalate (PET) film (100 μm thickness) was placed on the PDMS substrate and cut with a UV laser (SAMD-03-F0103, DPSS) to form outer and inner masks. The LM (Galinstan, 68.5% Ga, 21.5% In, 10% Sn, Geratherm Medical AG, Geschwenda) was then spray-printed onto the PDMS substrate to create soft circuits. (**ii**) The inner PET mask was removed to expose the area where modulus adjustment was required. A curing agent solution was applied to this area at a ratio of 1 μL mm^{-2} to modify its cross-linking density. The substrate was then fully cured at 70°C for 2 hours to form the bottom MG-PDMS structure. After peeling off the outer mask, the component was positioned on the modulus-adjusted region and connected to the LM circuit. Copper films (100 nm thickness) were added to the LM circuit to form the electrical interface. (**iii**) PDMS (20:1) was reapplied to encapsulate the components and semi-cured at 70°C for 20 minutes. A hollow PET mask was then placed on the top PDMS substrate, and the curing agent was dispensed to adjust the modulus gradient further, forming the top MG-PDMS. (**iv**) The entire device was fully cured in the oven at 70°C for 2 hours.

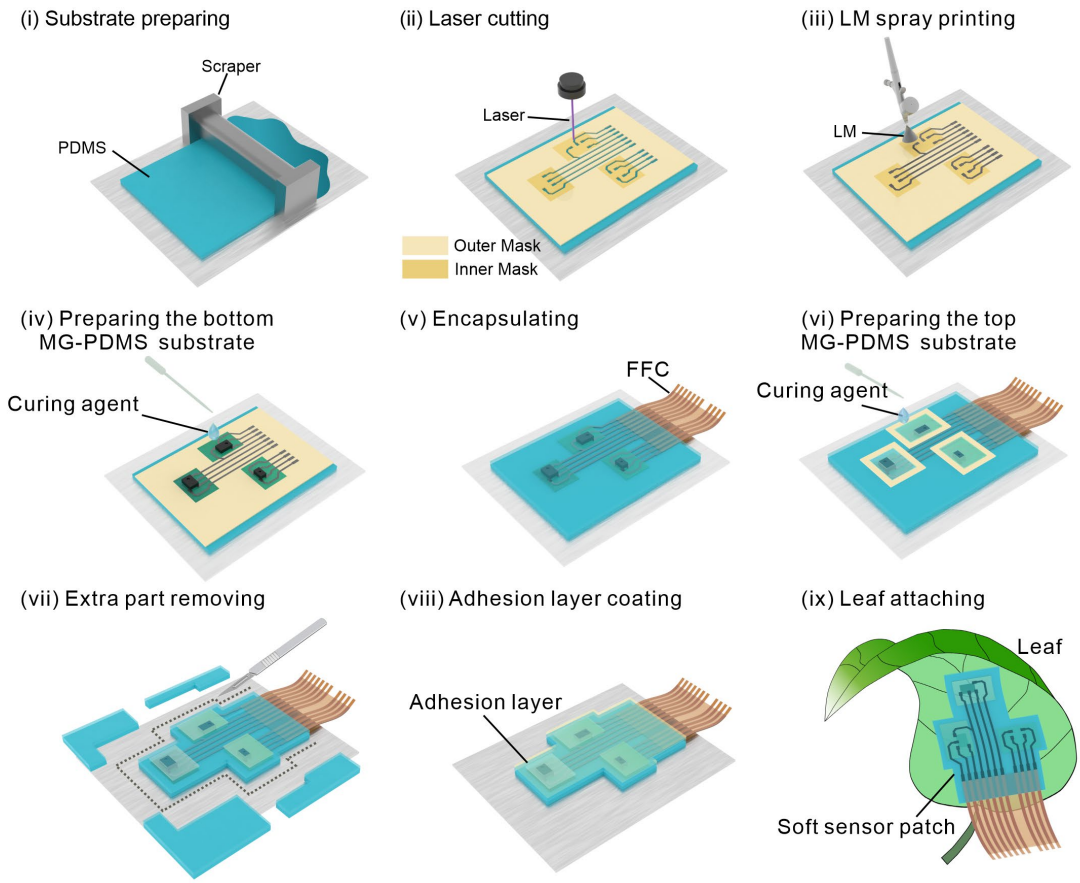

Fig. S35. Fabrication process schematics of the soft sensor patch. The whole fabrication process can be concluded into the following steps: (**i**) A PDMS substrate (about 250 μm thickness) was coated onto an aluminum plate using a scraper and heated to achieve a semi-cured status. (**ii**) Circuit patterns are laser cut into PET masks. (**iii**) LM was spray-printed onto the PET mask to create a circuit layout. (**iv**) The sensor components were soldered on small FPCB pads to extend their pins, making them more accessible to align with the LM circuit. A curing agent was then applied near the components to enhance the modulus of the substrate, forming the bottom MG-PDMS layer. (**v**) After removing the outer PET mask, the flexible flat cable (FFC) was connected to the LM circuits to form an electrical interface. The device was further encapsulated with PDMS and heated until the encapsulation layer became semi-cured. (**vi**) The curing agent was dropped into the hollow PET masks to create the top MG-PDMS substrate. (**vii**) Excess encapsulation material was trimmed away. (**viii**) An adhesive layer (S3-PDMS) was coated onto the encapsulated substrate. The device was subsequently heated at 90 °C for 3 hours to cure the adhesive layer. (**ix**) The soft sensor patch was attached to the abaxial surface of a tomato leaf.

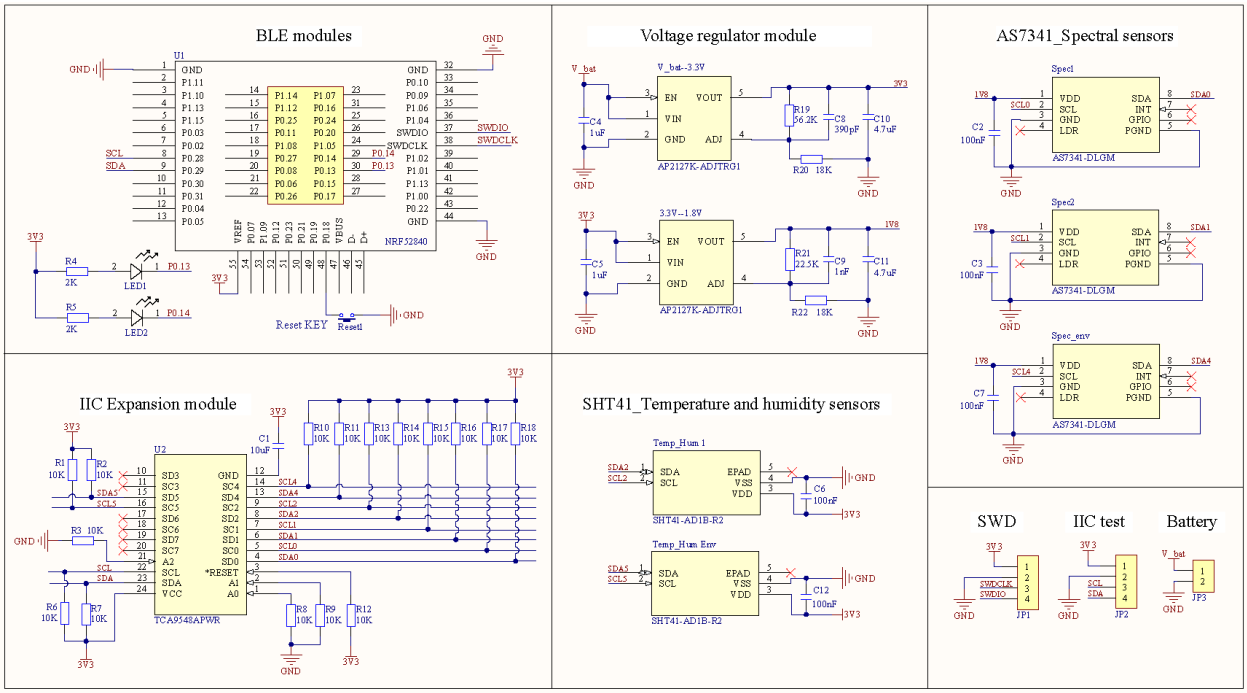

Fig. S36. Schematics of the hardware circuits.

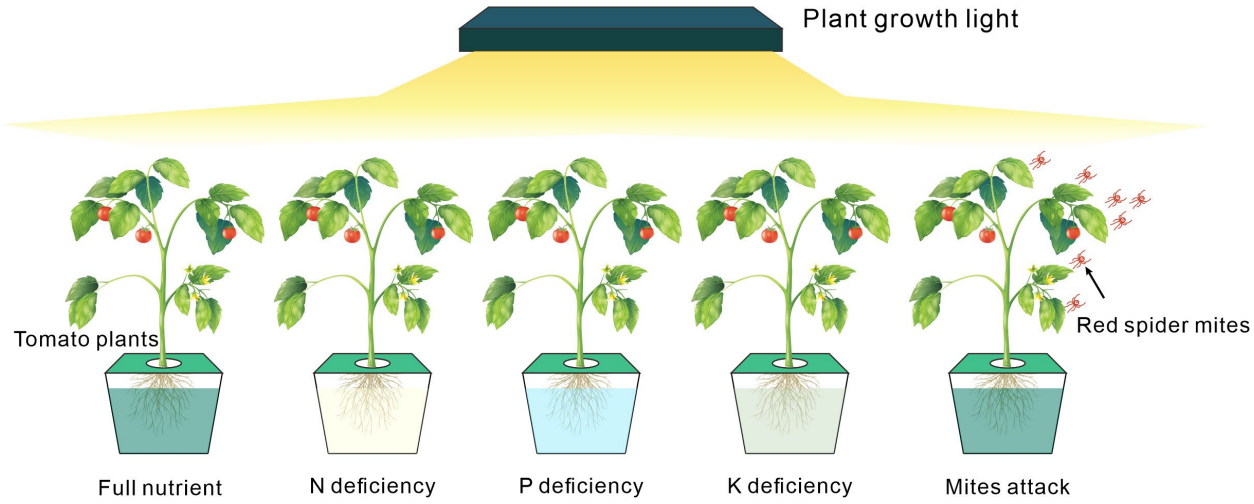

Fig. S37. Schematic of tomato plants cultivation environment.

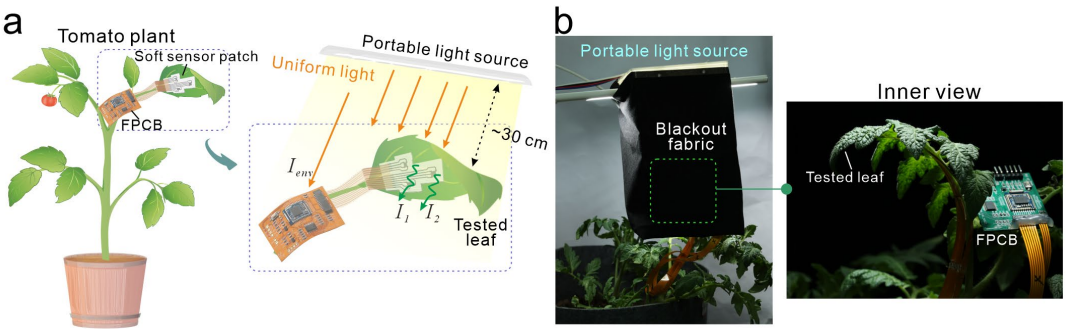

Fig. S38. Incident light setup for data collection. (**a**) Schematic and (**b**) Photos illustrating the measurement setup. During data collection, a portable light source is positioned approximately 30 cm above the tested leaf. A blackout fabric hood is used to block external light interference, ensuring consistent and reliable spectral data collection.

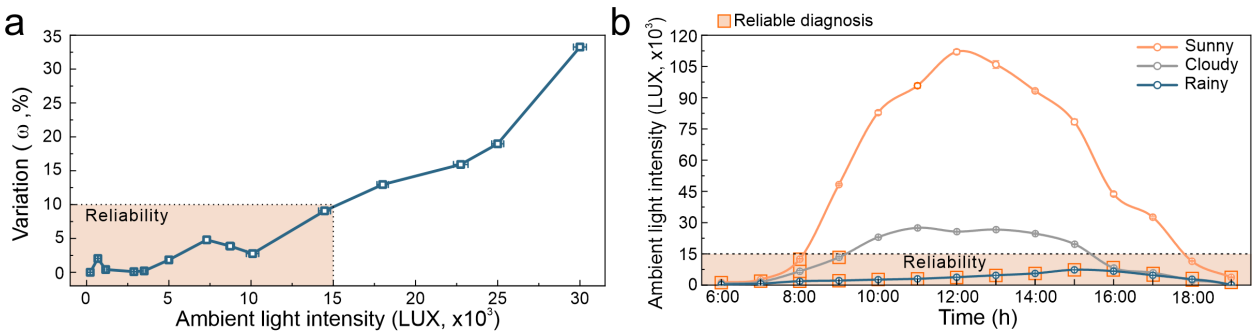

Fig. S39. Diagnostic stability of the MapS-Wear under various external light intensities. (**a**) Diagnostic variation across different light intensities, using healthy leaves as examples. The variation (ω) is calculated as: $\omega = (P_{\{i\}} - P_{\{0\}})/P_{\{0\}}$, where $P_{\{0\}}$ and $P_{\{i\}}$ represent the probability of the leaf being diagnosed as healthy by MapS-Wear under dark conditions and different external light intensities, respectively. When ω exceeds 10%, the diagnostic accuracy is significantly affected, indicating that MapS-Wear is unable to provide reliable diagnoses. (**b**) Diagnostic performance of MapS-Wear under different outdoor weather conditions (sunny, cloudy, and rainy). The orange shading indicates periods when MapS-Wear provides reliable diagnoses under moderate sunlight.

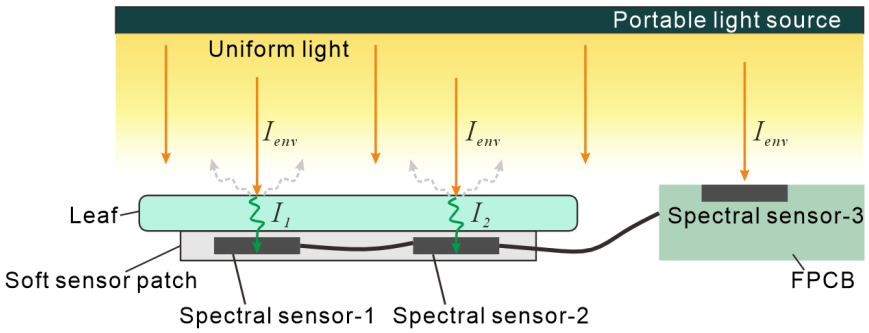

Fig. S40. Schematic of leaf's spectral transmittance data collection. The tested leaf is placed under a light box emitting stable parallel light. The soft sensor patch is attached to the lower epidermis of the leaf to collect two transmission spectra (I_1, I_2). Simultaneously, the environmental incidence light (I_{env}) is also recorded.

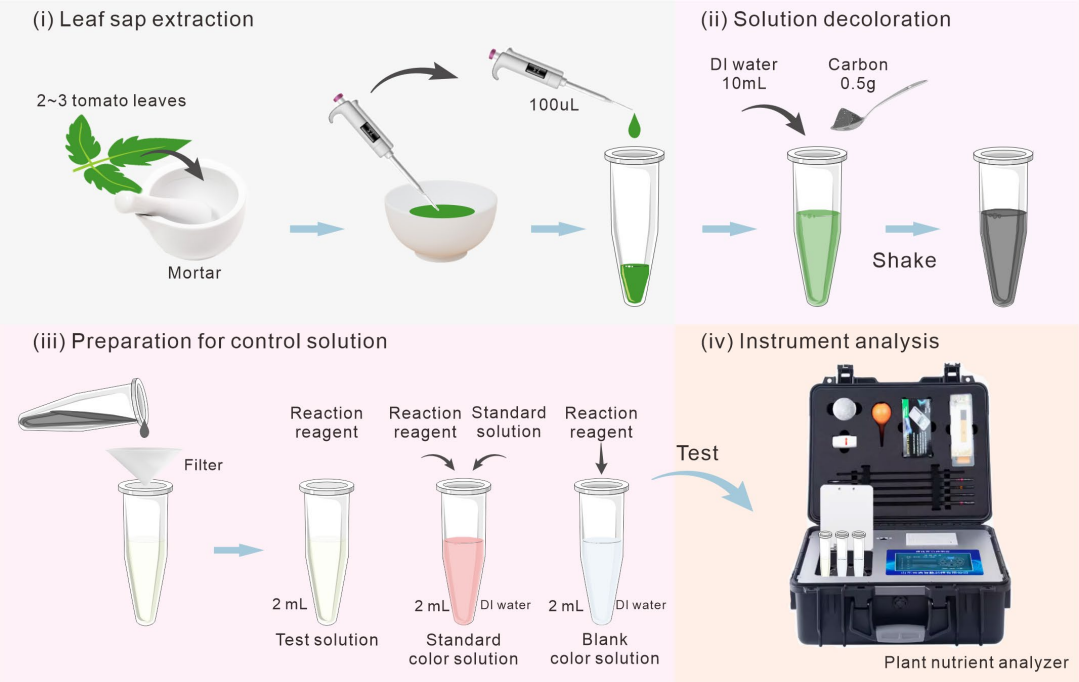

Fig. S41. Schematic process of nutrient content measurement via sap analysis. (**i**) Two to three fresh leaves were collected from tomato plants by using scissors. The leaves were pressed using a mortar to extract the sap. Then, 100 µL of sap was transferred into a plastic centrifuge tube using a pipette (4640040, Thermo Fisher Scientific). (**ii**) 10 mL of deionized (DI) water and 0.5 g of nanocarbon particles (100 nm diameter) were added to the tube to decolor the sap solution. (**iii**) The solution was shaken thoroughly for clarification and filtered through qualitative filter paper to obtain a clarified solution. Three types of solutions were prepared for control measurements: the test solution, the standard color solution, and the blank color solution. To prepare the test solution, 2 mL of clarified sap was mixed with the appropriate reaction reagent (specific to the nutrient type) in a tube for the color reaction. The standard color solution was prepared by combining the response reagent with a standard nutrient content solution and 2 mL of deionized (DI) water in a tube. The blank color solution, serving as a control, was prepared by adding only the reaction reagent to 2 mL of DI water. (**iv**) The prepared solutions were transferred to cuvettes and analyzed using a sap analyzer (YT-TR-ZY, YunTang). [Photo credit: Q.J. and X.Z., HUST]

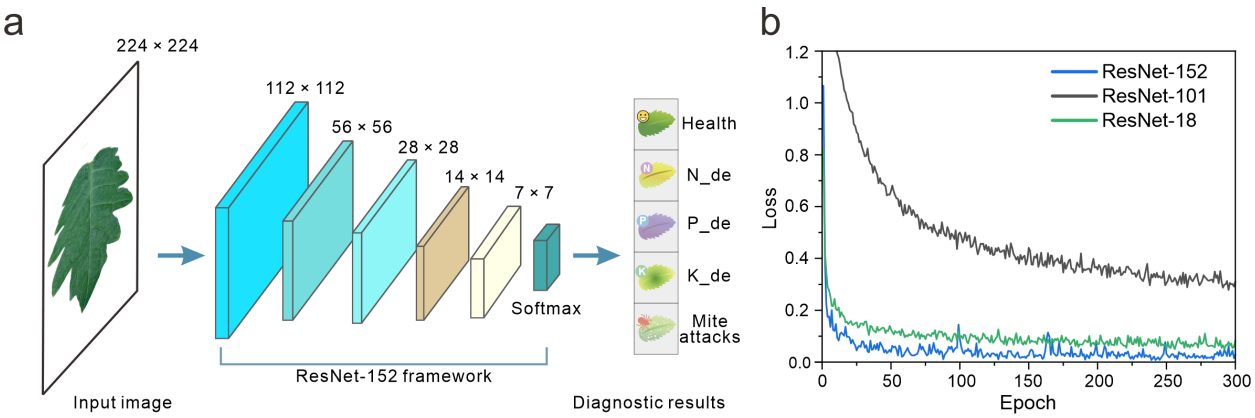

Fig. S42. Design of the CV framework. (**a**) Schematic of the diagnostic process of the ResNet-based CV framework. (**b**) The loss curve under different training epochs using various ResNet pre-train models, showing the ResNet-152 achieves the lowest loss after 300 epochs.

Experimental details: A total of 500 RGB images of leaves under various stress conditions were captured for CV training. Each image had its background removed and was scaled to a uniform size of 1500×1000 pixels. Through data augmentation, the training set was expanded to 2500 images. Subsequently, the entire photo dataset was split into training and test sets at a ratio of 0.8:0.2. The leaf image was resized into 224×224 for model input. The pre-trained ResNet-152 model, augmented with five fully connected layers, was used as the CV framework. The training was conducted on an Nvidia GeForce RTX 3090, with cross-entropy loss minimized using the Adam optimizer (learning rate: 0.0001). The batch size was set to 32, and the model was trained for 300 epochs.

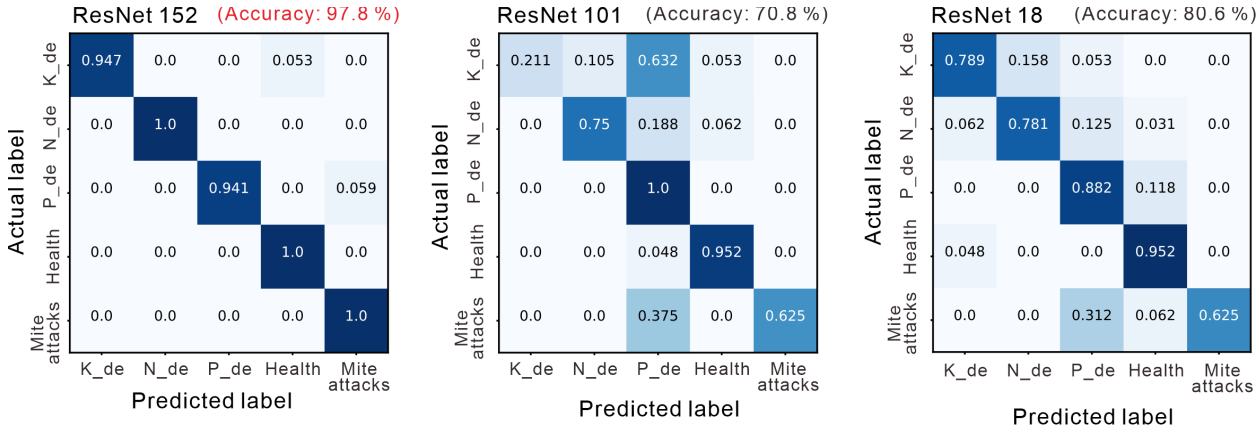

Fig. S43. Confusion matrix illustrating the performance of the CV method using different frameworks. The result shows that the ResNet-152-based framework achieves the highest prediction accuracy among other frameworks.

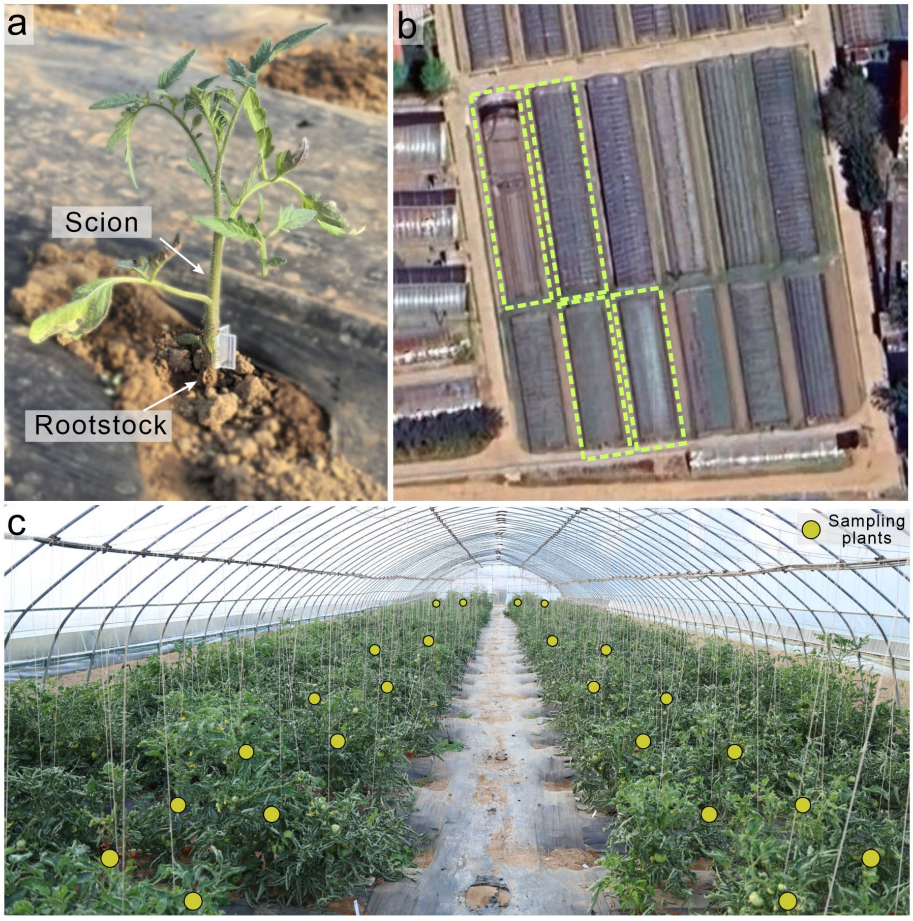

Fig. S44. Cultivating environment of grafted tomatoes. (**a**) Photo of the grafted tomato seedling being transplanted to the soil. (**b**) Map showing the cultivation environment of grafted tomatoes. Sample collection was conducted in greenhouses highlighted by yellow dashed boundary lines. (**c**) Photos illustrating the high-throughput screening of grafted varieties within greenhouse settings. [Photo credit: Q.J., HUST]

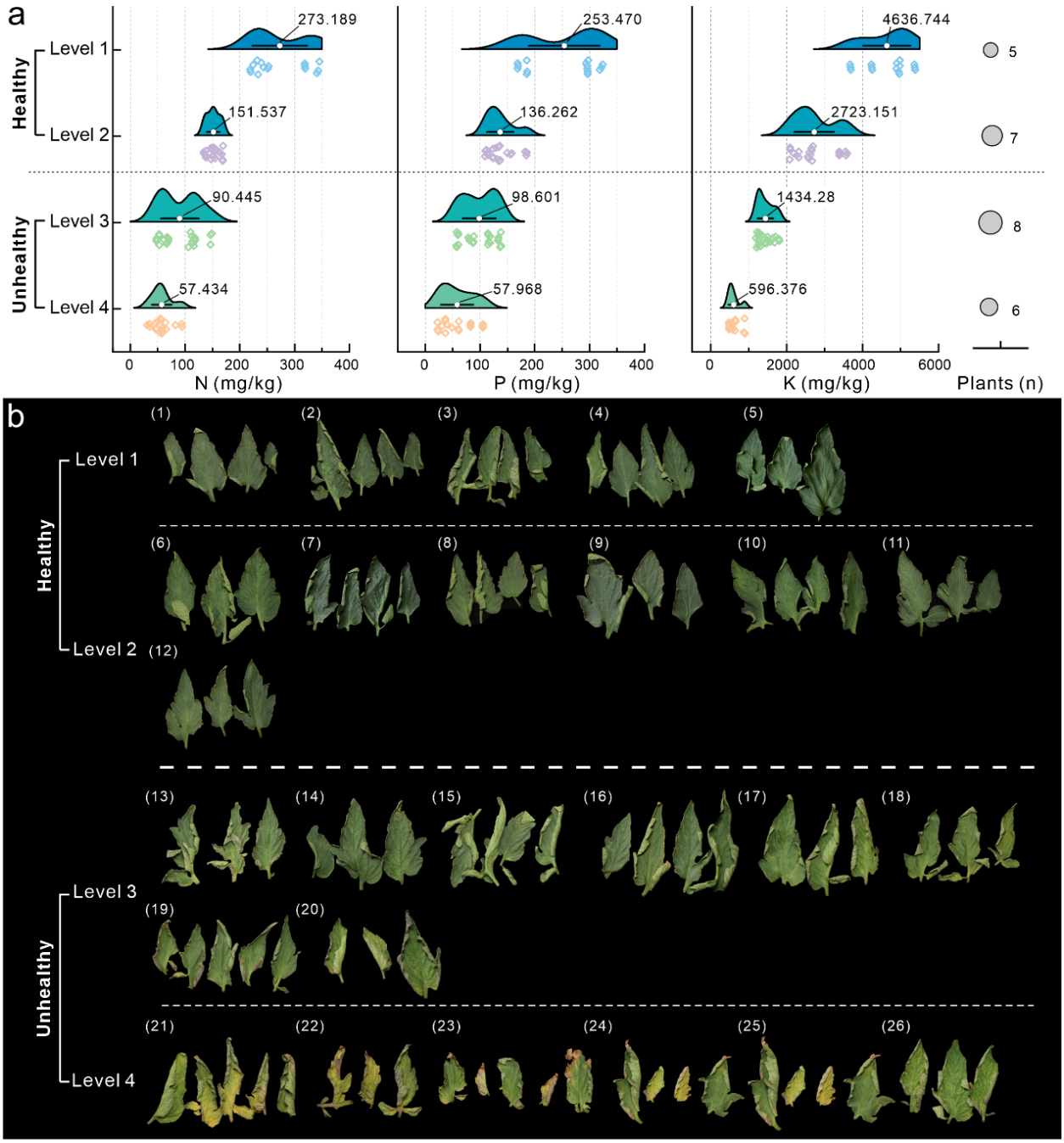

Fig. S45. Health Levels of Leaves in the Greenhouse. (**a**) Raincloud plot showing nutrient content (N, P, K) corresponding to different health levels of plants. The center circle indicates the mean value (labeled), the black line shows the standard deviation range, hollow dot presents the raw data. Plant sampling numbers for each health level are provided. (**b**) Photos of leaves classified into health levels 1–4, illustrating the progressive deterioration of the leaf health status. [Photo credit: Q.J., HUST]

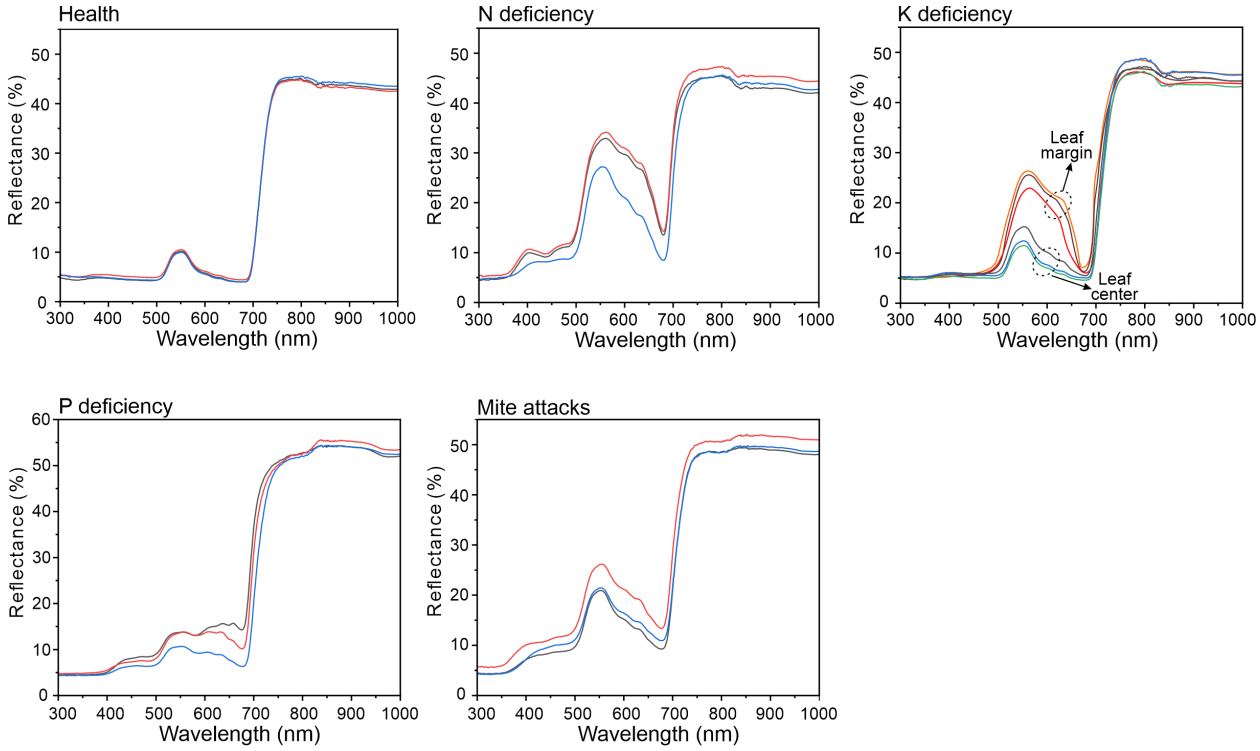

Fig. S46. Spectral reflectance of leaves in various health statuses.

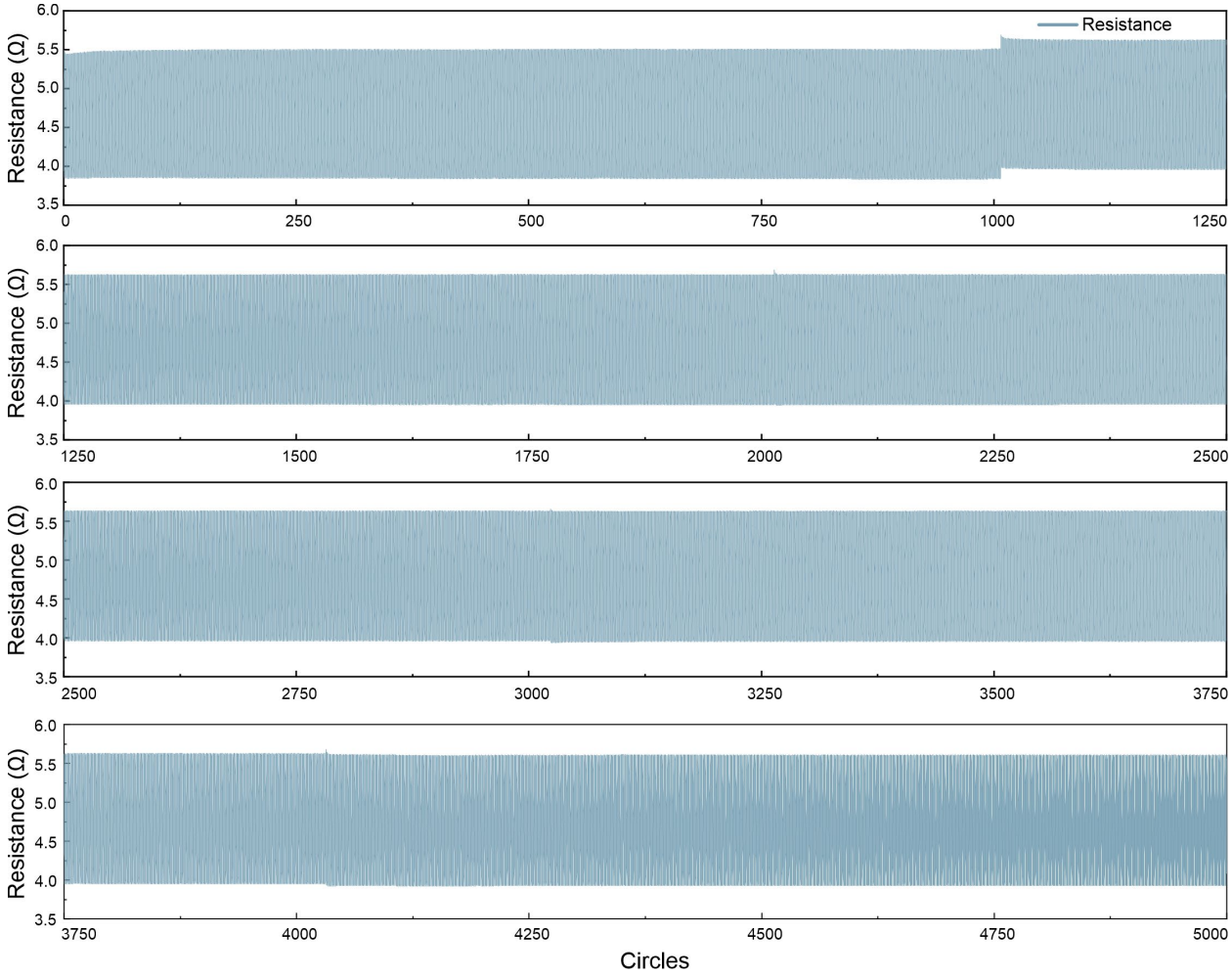

Fig. S47. Details of the 5000-cycling strain test of MG-PDMS structure. The MG-PDMS structure integrated with a resistor (3 Ω) is subjected to a 5000-cycle strain test at 50% strain and a frequency of 0.5 Hz.

Table S1. Comparison of different methods for tomato plant stress diagnosis.

Methods	Ref.	Accuracy	Samples number	Classifications	Classification of diseases	Algorithms
CV	(*50*)	98.4 %	18160	10	Health, bacterial Spot, Early Blight, etc.	CNN
	(*51*)	99.53 %	7000	3	Early Blight, Septoria Leaf Spot, Yellow Leaf Curl Virus	DCNN, ResNet-50
	(*52*)	99.98 %	6218	5	Health, Late Blight, Bacterial Spot, etc.	ICRMBO-CNN +VGG16
	(*53*)	92.5 %	8927	11	Health, Leaf Mold, Gray Mold, etc.	Deep Neural Network + LSTM
	(*54*)	98.19 %	16012	10	Bacterial spot, Early blight, Late blight, etc.	TomConv
	(*55*)	97.11 %	16012	10	Bacterial spot, Early blight, Late blight, etc.	C-GAN
Spectroscopy	(*56*)	90.7 %	354	2	Bacterial Wilt, Healthy	GA+SVM
	(*57*)	85 %	3478	3	Pst, Xeu, Healthy	SVM
	(*58*)	91.6 %	284	2	S. sclerotiorum Disease, Healthy	SNV-SVM
	(*59*)	92 %	3877	6	Anthracnose, Early Blight, Healthy, etc.	Ridge classifier
VOC	(*60*)	86.7 %	60	2	Health, Aphid Infestation	PCA
	(*61*)	87.4 %	30	2	Healthy, Whitefly Infestation	PCA, HCA
	(*62*)	95.4 %	65	4	Health, P. infestans, Early Blight, Septoria Leaf Spot	PCA
	(*63*)	95.7 %	147	4	Health, P. infestans, Gray Mold, Early Blight	PCA
This work		**99.2 %**	**500**	**7**	**Health, Drought, Heat, N, P, K deficiencies, Spider mites attack**	**Ensemble learning**

Table S2. Diagnostic result of healthy status of grafted tomato from sap analysis and MapS-Wear. If the diagnostic categories identified by MapS-Wear align with those from sap analysis, the result is recorded as "Yes" for accuracy.

Plant	Sap analysis result	MapS-Ware diagnostic result	Accuracy	Plant	Sap analysis result	MapS-Ware diagnostic result	Accuracy	Plant	Sap analysis result	MapS-Ware diagnostic result	Accuracy
#1	Health	Health	√Yes	**#18**	N, P deficiencies	N deficiency	√Yes	**#35**	Health	K, N deficiencies	**×No**
#2	Health	Health	√Yes	**#19**	Health	Health	√Yes	**#36**	Health	Health	√Yes
#3	Health	Health	√Yes	**#20**	Health	N, K deficiencies	**×No**	**#37**	N, P, K deficiencies	K deficiency	√Yes
#4	N, P, K deficiencies	N, P, K deficiencies	√Yes	**#21**	Health	Health	√Yes	**#38**	N, P, K deficiencies	N, K deficiencies	√Yes
#5	Health	K deficiency	**×No**	**#22**	Health	Health	√Yes	**#39**	N deficiency	K deficiency, Health	**×No**
#6	Health	Health	√Yes	**#23**	P, K deficiencies	P, K deficiencies	√Yes	**#40**	N, P, K deficiencies	K, N deficiencies	√Yes
#7	Health	Health	√Yes	**#24**	N, P, K deficiencies	K deficiency	√Yes	**#41**	Health	Health	√Yes
#8	Health	Health	√Yes	**#25**	K deficiency	K deficiency	√Yes	**#42**	Health	K deficiency	**×No**
#9	N, P, K deficiencies	N, K deficiencies	√Yes	**#26**	P, K deficiencies	K deficiency	√Yes	**#43**	N, K deficiencies	N, K deficiencies	√Yes
#10	N, P, K deficiencies	N, P, K deficiencies	√Yes	**#27**	Health	Health	√Yes	**#44**	Health	Health	√Yes
#11	N, P, K deficiencies	N, K deficiencies	√Yes	**#28**	N, P, K deficiencies	K deficiency	√Yes	**#45**	N, K deficiencies	N, K deficiencies	√Yes
#12	N, P, K deficiencies	N, K deficiencies	√Yes	**#29**	Health	Health	√Yes	**#46**	N, K deficiencies	N, K deficiencies	√Yes
#13	N, P, K deficiencies	K deficiency	√Yes	**#30**	P, K deficiencies	K deficiency	√Yes	**#47**	N, P, K deficiencies	N, K deficiencies	√Yes
#14	N, P, K deficiencies	N, K deficiencies	√Yes	**#31**	N, P, K deficiencies	N, K deficiencies	√Yes	**#48**	Health	K deficiency	**×No**
#15	N, P, K deficiencies	K deficiency	√Yes	**#32**	N, P, K deficiencies	N, K deficiencies	√Yes	**#49**	N deficiency	N deficiency	√Yes
#16	N, P, K deficiencies	K deficiency	√Yes	**#33**	N, P, K deficiencies	N deficiency	√Yes	**#50**	N, P, K deficiencies	K deficiency	√Yes
#17	N, P, K deficiencies	N, K deficiencies	√Yes	**#34**	P, K deficiencies	K deficiency	√Yes				

Table S3. Comparison of various soft wearable sensors for plant stress diagnosis.
Abbreviations: Humidity (Hum.), Temperature (Temp.).

References	**This work**	(*37*)	(*35*)	(*41*)	(*33*)	(*32*)	(*34*)
Plant	**Tomato**	14 plants	4 plants	2 plants	Tomato	Tomato	3 plants
Physiological information	**Temp., Hum., Transmission spectra**	Bioimpedance	Temp., Strain	Bioimpedance	Temp., Hum., VOCs	VOCs	Spectral reflectance
Stress types	**7 types** (Biotic, Abiotic) Health, Drought, Heat, Senescence, Deficiencies of N, P, K, Mite attacks	2 types (Abiotic) Drought, Photodamage	2 types (Abiotic) Heat, Drought	3 types (Abiotic) Heat, Drought, Ultraviolet A irradiation	6 types (Biotic, Abiotic) Mechanical injury, Drought, Overwatering, Salinity, Dark, Pathogenic infection	2 types (Biotic, Abiotic) Late blight, Mechanical damage	2 types (Biotic, Abiotic) Virus, Dark
Early diagnosis time	**10 days (Compared to CV method)**	—	—	—	2~3 days (Compared to visual assessment)	4 days (Compared to visual assessment)	4 days (Compared to visual color difference)
Diagnostic method	**Machine learning**	Manual analysis	Manual analysis	Manual analysis	PCA + Manual analysis	PCA + Manual analysis	Manual analysis
Diagnostic accuracy	**99.2%**	—	—	—	77.4 % (Explained variance ratio)	97 % (Explained variance ratio)	—
Result output	**Real-time**	Off-line	Off-line	Off-line	Off-line	Off-line	Off-line

Table S4. The overall hardware cost of the MapS-Wear.

Class	Quantity	Cost ($)
Components (Resistor, capacity, etc.)	42	0.5
BLE microcontroller (NRF52840)	1	10
T&H sensor (SHT41)	2	1.5
Spectral sensor (AS7341)	3	13
FPCB	1	3.5
FFC	1	0.5
PDMS+LM	—	1
Total		**30**

Table S5. Details of prediction probability function in different estimators.

Estimators	Prediction probability functions	Parameters explanation
Logistic Regression (LR)	$P(k \mid x) = \frac{1}{1+\exp(-(\mathbf{w}^{\top}\mathbf{x}+b))}$	$\mathbf{w}$: Weight vector. b: Bias term. $\mathbf{x}$: Input feature vector. $\mathbf{exp}$: Exponential function.
Decision Tree (DT)	$P(k \mid x) = \frac{N_k}{N}$	N_k: Number of training samples of class k in the leaf node where $\mathbf{x}$ falls. N: Total number of training samples in that leaf node.
Random Forest (RF)	$P(k \mid x) = \frac{1}{T}\sum_{t=1}^{T} P_t(k \mid x)$	T: Total number of trees in the forest. $P_t(k \mid x)$: Probability estimate for class k from the t-th tree.
Extra Trees (ET)	$P(k \mid x) = \frac{1}{T}\sum_{t=1}^{T} P_t(k \mid x)$	T: Total number of trees in the ensemble. $P_t(k \mid x)$: Probability estimate for class k from the t-th tree.
AdaBoost	$P(k \mid x) = \frac{\exp(F_k(\mathbf{x}))}{\sum_{j=1}^{K}\exp(F_j(\mathbf{x}))}$, where $F_k(\mathbf{x}) = \sum_{t=1}^{T}\alpha_t\, h_t^k(\mathbf{x})$	$F_k(\mathbf{x})$: Weighted sum of weak classifiers' outputs for class k. T: Total number of weak classifiers. α_t: Weight assigned to the t-th weak classifier. $h_t^k(\mathbf{x})$: Output of the t-th weak classifier for class k.
Gradient Boosting (GB)	$P(k \mid x) = \frac{\exp(F_k(\mathbf{x}))}{\sum_{j=1}^{K}\exp(F_j(\mathbf{x}))}$, where $F_k(\mathbf{x}) = F_{k,0} + \sum_{t=1}^{T} f_{t,k}(\mathbf{x})$	$F_k(\mathbf{x})$: Accumulated prediction for class k. $F_{k,0}$: Initial prediction, often set to a constant. T: Total number of boosting iterations. $f_{t,k}(\mathbf{x})$: Output of the t-th weak learner for class k.
Support Vector Classifier (SVC)	$P(k \mid x) = \frac{1}{1+\exp(Af(\mathbf{x})+B)}$	$f(\mathbf{x})$: Decision function output for input $\mathbf{x}$. A: Parameter learned during Platt scaling. B: Parameter learned during Platt scaling.

Table S6. Performance evaluation of SDM and other deep learning methods.

Model	Accuracy	F1-score	10-fold cross-validation	Characteristics	Training time (s)
CNNs	97.13%	98.19%	94.73%	Overfitting	35.67 (150 epochs)
LSTMs	84.89%	84.66%	69.54%	Underfitting	61.44 (150 epochs)
Bi-LSTMs	81.21%	80.60%	71.52%	Underfitting	81.5 (150 epochs)
SDM(Ours)	**99.20%**	**99.69%**	**99.09%**	**Balanced**	**1.81**

Supplementary Movies (separate files)

Movie S1. An introduction of the MapS-Wear.

This video illustrates the design and working principle of MapS-Wear, the development of the ML-powered diagnostic framework, and the system's application from lab validation to agricultural implementation.

Movie S2. Attachment of the soft sensor patch to a tomato leaf.

This video demonstrates the process for attaching the soft sensor patch to the abaxial surface of a live tomato leaf.

Movie S3. Real-time diagnosis of tomato leaves under various health statuses.

This video demonstrates a real-time diagnosis of tomato leaves under various health statuses, including health, nutrient deficiencies (N, K, P), and mite attacks.

Movie S4. Graft compatibility evaluation of grafted tomatoes in greenhouses.

This video demonstrates large-scale compatibility evaluations of grafted tomatoes in greenhouses using the MapS-Wear.

REFERENCES AND NOTES

1. FAO, IFAD, UNICEF, WFP, WHO, "*The State of Food Security and Nutrition in the World 2023*" (2023); www.fao.org/documents/card/en/c/cc3017en.

2. D. Headey, M. Ruel, Food inflation and child undernutrition in low and middle income countries. *Nat. Commun.* **14**, 5761 (2023).

3. P. G. Kopelman, Obesity as a medical problem. *Nature* **404**, 635–643 (2000).

4. A. Fardet, Y. Boirie, Associations between food and beverage groups and major diet-related chronic diseases: An exhaustive review of pooled/meta-analyses and systematic reviews. *Nutr. Rev.* **72**, 741–762 (2014).

5. D. Bhowmik, K. S. Kumar, S. Paswan, S. Srivastava, Tomato-a natural medicine and its health benefits. *J. Pharmacogn. Phytochem.* **1**, 33–43 (2012).

6. FAO, *Agricultural production statistics 2000–2022* (FAOSTAT Analytical Briefs, no. 79, 2023); https://doi.org/10.4060/cc9205en.

7. S. Panno, S. Davino, A. G. Caruso, S. Bertacca, A. Crnogorac, A. Mandić, E. Noris, S. Matić, A review of the most common and economically important diseases that undermine the cultivation of tomato crop in the mediterranean basin. *Agronomy* **11**, 2188 (2021).

8. M. C. Picanço, L. Bacci, A. L. B. Crespo, M. M. M. Miranda, J. C. Martins, Effect of integrated pest management practices on tomato production and conservation of natural enemies. *Agri. For. Entomol.* **9**, 327–335 (2007).

9. M. Alsamir, T. Mahmood, R. Trethowan, N. Ahmad, An overview of heat stress in tomato (*Solanum lycopersicum* L.). *Saudi J. Biol. Sci.* **28**, 1654–1663 (2021).

10. R. Zhou, X. Yu, C.-O. Ottosen, E. Rosenqvist, L. Zhao, Y. Wang, W. Yu, T. Zhao, Z. Wu, Drought stress had a predominant effect over heat stress on three tomato cultivars subjected to combined stress. *BMC Plant Biol.* **17**, 24 (2017).

11. S. Fahad, O. Sönmez, S. Saud, D. Wang, C. Wu, M. Adnan, M. Arif, Amanullah, *Engineering Tolerance in Crop Plants Against Abiotic Stress* (CRC Press, ed. 1, 2021); www.taylorfrancis.com/books/9781003160717).

12. A. Migeon, F. Ferragut, L. A. Escudero-Colomar, K. Fiaboe, M. Knapp, G. J. De Moraes, E. Ueckermann, M. Navajas, Modelling the potential distribution of the invasive tomato red spider mite, Tetranychus evansi (Acari: Tetranychidae). *Exp. Appl. Acarol.* **48**, 199–212 (2009).

13. A. H. Molla, M. Manjurul Haque, M. Amdadul Haque, G. N. M. Ilias, Trichoderma-enriched biofertilizer enhances production and nutritional quality of tomato (*Lycopersicon esculentum* Mill.) and minimizes NPK fertilizer use. *Agric. Res.* **1**, 265–272 (2012).

14. W. W. Adams III, I. Terashima, The Leaf: A platform for performing photosynthesis, in *Advances in Photosynthesis and Respiration* (Springer International Publishing, 2018), vol. 44; http://link.springer.com/10.1007/978-3-319-93594-2.

15. Q. Liu, C. Zhang, H. Fang, L. Yi, M. Li, Indispensable biomolecules for plant defense against pathogens: NBS-LRR and “nitrogen pool” alkaloids. *Plant Sci.* **334**, 111752 (2023).

16. A. Künstler, G. Gullner, A. L. Ádám, J. K. Kolozsváriné Nagy, L. Király, The versatile roles of sulfur-containing biomolecules in plant defense—A road to disease resistance. *Plants* **9**, 1705 (2020).

17. H. Yin, Y. Cao, B. Marelli, X. Zeng, A. J. Mason, C. Cao, Soil sensors and plant wearables for smart and precision agriculture. *Adv. Mater.* **33**, 2007764 (2021).

18. A. V. Zubler, J.-Y. Yoon, Proximal methods for plant stress detection using optical sensors and machine learning. *Biosensors* **10**, 193 (2020).

19. G. Kitić, A. Tagarakis, N. Cselyuszka, M. Panić, S. Birgermajer, D. Sakulski, J. Matović, A new low-cost portable multispectral optical device for precise plant status assessment. *Comput. Electron. Agric.* **162**, 300–308 (2019).

20. D. Tholl, O. Hossain, A. Weinhold, U. S. R. Röse, Q. Wei, Trends and applications in plant volatile sampling and analysis. *Plant J.* **106**, 314–325 (2021).

21. Z. Tian, W. Ma, Q. Yang, F. Duan, Application status and challenges of machine vision in plant factory—A review. *Inf. Process Agric.* **9**, 195–211 (2022).

22. A. Lowe, N. Harrison, A. P. French, Hyperspectral image analysis techniques for the detection and classification of the early onset of plant disease and stress. *Plant Methods* **13**, 80 (2017).

23. H. J. Butler, M. R. McAinsh, S. Adams, F. L. Martin, Application of vibrational spectroscopy techniques to non-destructively monitor plant health and development. *Anal. Methods* **7**, 4059–4070 (2015).

24. S. Ghosal, D. Blystone, A. K. Singh, B. Ganapathysubramanian, A. Singh, S. Sarkar, An explainable deep machine vision framework for plant stress phenotyping. *Proc. Natl. Acad. Sci. U.S.A.* **115**, 4613–4618 (2018).

25. Y. Yan, M. Ni, F. Wang, Y. Yu, X. Gong, Y. Huang, W. Tao, C. Li, F. Wang, Metal–organic framework-based biosensor for detecting hydrogen peroxide in plants through color-to-thermal signal conversion. *ACS Nano* **16**, 15175–15187 (2022).

26. A. Singh, B. Ganapathysubramanian, A. K. Singh, S. Sarkar, Machine learning for high-throughput stress phenotyping in plants. *Trends Plant Sci.* **21**, 110–124 (2016).

27. J. J. Walsh, E. Mangina, S. Negrão, Advancements in imaging sensors and AI for plant stress detection: A systematic literature review. *Plant Phenomics* **6**, 0153 (2024).

28. S. A. D. M. Zahir, M. F. Jamlos, A. F. Omar, M. A. Jamlos, R. Mamat, J. Muncan, R. Tsenkova, Review–Plant nutritional status analysis employing the visible and near-infrared spectroscopy spectral sensor. *Spectrochim. Acta A. Mol. Biomol. Spectrosc.* **304**, 123273 (2024).

29. D. Son, J. Park, S. Lee, J. J. Kim, S. Chung, Integrating non-invasive VIS-NIR and bioimpedance spectroscopies for stress classification of sweet basil (*Ocimum basilicum* L.) with machine learning. *Biosens. Bioelectron.* **263**, 116579 (2024).

30. Y. Chai, C. Chen, X. Luo, S. Zhan, J. Kim, J. Luo, X. Wang, Z. Hu, Y. Ying, X. Liu, Cohabiting plant-wearable sensor in situ monitors water transport in plant. *Adv. Sci.* **8**, 2003642 (2021).

31. J. A. Barbosa, V. M. S. Freitas, L. H. B. Vidotto, G. R. Schleder, R. A. G. De Oliveira, J. F. Da Rocha, L. T. Kubota, L. C. S. Vieira, H. C. N. Tolentino, I. T. Neckel, A. L. Gobbi, M. Santhiago, R. S. Lima, Biocompatible wearable electrodes on leaves toward the on-site monitoring of water loss from plants. *ACS Appl. Mater. Interfaces* **14**, 22989–23001 (2022).

32. Z. Li, Y. Liu, O. Hossain, R. Paul, S. Yao, S. Wu, J. B. Ristaino, Y. Zhu, Q. Wei, Real-time monitoring of plant stresses via chemiresistive profiling of leaf volatiles by a wearable sensor. *Matter* **4**, 2553–2570 (2021).

33. G. Lee, O. Hossain, S. Jamalzadegan, Y. Liu, H. Wang, A. C. Saville, T. Shymanovich, R. Paul, D. Rotenberg, A. E. Whitfield, J. B. Ristaino, Y. Zhu, Q. Wei, Abaxial leaf surface-mounted multimodal wearable sensor for continuous plant physiology monitoring. *Sci. Adv.* **9**, eade2232 (2023).

34. K. Zhang, W. Li, H. Li, Y. Luo, Z. Li, X. Wang, X. Chen, A leaf-patchable reflectance meter for in situ continuous monitoring of chlorophyll content. *Adv. Sci.* **10**, 20232305552 (2023).

35. Y. Yang, T. He, P. Ravindran, F. Wen, P. Krishnamurthy, L. Wang, Z. Zhang, P. P. Kumar, E. Chae, C. Lee, All-organic transparent plant e-skin for noninvasive phenotyping. *Sci. Adv.* **10**, eadk7488 (2024).

36. C. Zhang, C. Zhang, X. Wu, J. Ping, Y. Ying, An integrated and robust plant pulse monitoring system based on biomimetic wearable sensor. *NPJ Flex. Electron.* **6**, 43 (2022).

37. J. J. Kim, L. K. Allison, T. L. Andrew, Vapor-printed polymer electrodes for long-term, on-demand health monitoring. *Sci. Adv.* **5**, eaaw0463 (2019).

38. J. J. Kim, R. Fan, L. K. Allison, T. L. Andrew, On-site identification of ozone damage in fruiting plants using vapor-deposited conducting polymer tattoos. *Sci. Adv.* **6**, eabc3296 (2020).

39. M. Jiang, S. Chen, P. Zhang, Y. Sun, J. Ye, Y. Deng, L. Li, J. Liu, Liquid metal enabled plant injectable electronics. *Mater. Today* **66**, 50–61 (2023).

40. E. Bihar, E. J. Strand, C. A. Crichton, M. N. Renny, I. Bonter, T. Tran, M. Atreya, A. Gestos, J. Haseloff, R. R. McLeod, G. L. Whiting, Self-healable stretchable printed electronic cryogels for in-vivo plant monitoring. *NPJ Flex Electron* **7**, 48 (2023).

41. Y. Lu, K. Xu, L. Zhang, M. Deguchi, H. Shishido, T. Arie, R. Pan, A. Hayashi, L. Shen, S. Akita, K. Takei, Multimodal plant healthcare flexible sensor system. *ACS Nano* **14**, 10966–10975 (2020).

42. J. A. Rogers, T. Someya, Y. Huang, Materials and mechanics for stretchable electronics. *Science* **327**, 1603–1607 (2010).

43. S. Xu, Y. Zhang, L. Jia, K. E. Mathewson, K.-I. Jang, J. Kim, H. Fu, X. Huang, P. Chava, R. Wang, S. Bhole, L. Wang, Y. J. Na, Y. Guan, M. Flavin, Z. Han, Y. Huang, J. A. Rogers, Soft microfluidic assemblies of sensors, circuits, and radios for the skin. *Science* **344**, 70–74 (2014).

44. J. K. Schjoerring, The molecular–physiological functions of mineral macronutrients and their consequences for deficiency symptoms in plants. *New Phytol.* **229**, 2446–2469 (2020).

45. G. A. Blackburn, Hyperspectral remote sensing of plant pigments. *J. Exp. Bot.* **58**, 855–867 (2006).

46. D. A. Sims, J. A. Gamon, Relationships between leaf pigment content and spectral reflectance across a wide range of species, leaf structures and developmental stages. *Remote Sens. Environ.* **81**, 337–354 (2002).

47. J. Zeng, W. Ping, A. Sanaeifar, X. Xu, W. Luo, J. Sha, Z. Huang, Y. Huang, X. Liu, B. Zhan, H. Zhang, X. Li, Quantitative visualization of photosynthetic pigments in tea leaves based on Raman spectroscopy and calibration model transfer. *Plant Methods* **17**, 4 (2021).

48. A. S. Parmagnani, G. Mannino, C. Brillada, M. Novero, L. Dall'Osto, M. E. Maffei, Biology of two-spotted spider mite (*Tetranychus urticae*): Ultrastructure, photosynthesis, guanine

transcriptomics, carotenoids and chlorophylls metabolism, and decoyinine as a potential acaricide. *Int. J. Mol. Sci.* **24**, 1715 (2023).

49. F. C. Meinzer, Stomatal control of transpiration. *Trends Ecol. Evol.* **8**, 289–294 (1993).

50. M. Agarwal, S. Kr Gupta, K. K. Biswas, Development of efficient CNN model for Tomato crop disease identification. *Sustain. Comput. Inform. Syst.* **28**, 100407 (2020).

51. M. I. Hossain, S. Jahan, M. R. Al Asif, M. Samsuddoha, K. Ahmed, Detecting tomato leaf diseases by image processing through deep convolutional neural networks. *Smart Agr. Technol.* **5**, 100301 (2023).

52. S. Nandhini, K. Ashokkumar, Improved crossover based monarch butterfly optimization for tomato leaf disease classification using convolutional neural network. *Multimed. Tools Appl.* **80**, 18583–18610 (2021).

53. A. Fuentes, S. Yoon, D. S. Park, Deep learning-based phenotyping system with glocal description of plant anomalies and symptoms. *Front. Plant Sci.* **10**, 1321 (2019).

54. P. Baser, J. R. Saini, K. Kotecha, TomConv: An improved CNN model for diagnosis of diseases in tomato plant leaves. *Procedia Comput. Sci.* **218**, 1825–1833 (2023).

55. A. Abbas, Tomato plant disease detection using transfer learning with C-GAN synthetic images. *Comput. Electron. Agric.* **187**, 106279 (2021).

56. Y. Cen, Y. Huang, S. Hu, L. Zhang, J. Zhang, Early detection of bacterial wilt in tomato with portable hyperspectral spectrometer. *Remote Sens.* **14**, 2882 (2022).

57. M. Reis Pereira, F. N. D. Santos, F. Tavares, M. Cunha, Enhancing host-pathogen phenotyping dynamics: Early detection of tomato bacterial diseases using hyperspectral point measurement and predictive modeling. *Front. Plant Sci.* **14**, 1242201 (2023).

58. Y. Zhou, J. Chen, J. Ma, X. Han, B. Chen, G. Li, Z. Xiong, F. Huang, Early warning and diagnostic visualization of Sclerotinia infected tomato based on hyperspectral imaging. *Sci. Rep.* **12**, 21140 (2022).

59. M. Tomaszewski, J. Nalepa, E. Moliszewska, B. Ruszczak, K. Smykała, Early detection of *Solanum lycopersicum* diseases from temporally-aggregated hyperspectral measurements using machine learning. *Sci. Rep.* **13**, 7671 (2023).

60. S. Cui, E. A. A. Inocente, N. Acosta, H. M. Keener, H. Zhu, P. P. Ling, Development of fast E-nose system for early-stage diagnosis of aphid-stressed tomato plants. *Sensors* **19**, 3480 (2019).

61. S. Cui, L. Cao, N. Acosta, H. Zhu, P. P. Ling, Development of portable E-nose system for fast diagnosis of whitefly infestation in tomato plant in greenhouse. *Chemosensors* **9**, 297 (2021).

62. Z. Li, R. Paul, T. Ba Tis, A. C. Saville, J. C. Hansel, T. Yu, J. B. Ristaino, Q. Wei, Non-invasive plant disease diagnostics enabled by smartphone-based fingerprinting of leaf volatiles. *Nat. Plants* **5**, 856–866 (2019).

63. H. Chen, Z. You, X. Wang, Q. Qiu, Y. Ying, Y. Wang, An artificial olfactory sensor based on flexible metal–organic frameworks for sensing VOCs. *Chem. Eng. J* **446**, 137098 (2022).

64. H. Singh, P. Kumar, S. Chaudhari, M. Edelstein, Tomato grafting: A global perspective. *Horts* **52**, 1328–1336 (2017).

65. J. D. H. Keatinge, L.-J. Lin, A. W. Ebert, W. Y. Chen, J. d.' A. Hughes, G. C. Luther, J.-F. Wang, M. Ravishankar, Overcoming biotic and abiotic stresses in the *Solanaceae* through grafting: Current status and future perspectives. *Biol. Agric. Hortic.* **30**, 272–287 (2014).

66. E. Sánchez-Rodríguez, R. Leyva, C. Constán-Aguilar, L. Romero, J. M. Ruiz, Grafting under water stress in tomato cherry: Improving the fruit yield and quality. *Ann. Appl. Biol.* **161**, 302–312 (2012).

67. M. Kawaguchi, A. Taji, D. Backhouse, M. Oda, Anatomy and physiology of graft incompatibility in solanaceous plants. *J. Hortic. Sci. Biotech.* **83**, 581–588 (2008).

68. M. P. Wolf, G. B. Salieb-Beugelaar, P. Hunziker, PDMS with designer functionalities—Properties, modifications strategies, and applications. *Prog. Polym. Sci.* **83**, 97–134 (2018).

69. J. Jiang, S. Zhang, B. Wang, H. Ding, Z. Wu, Hydroprinted liquid-alloy-based morphing electronics for fast-growing/tender plants: From physiology monitoring to habit manipulation. *Small* **16**, 2003833 (2020).

70. R. Pearcey, H. Mooney, P. Rundel, *Plant Physiological Ecology: Field Methods and Instrumentation* (Springer Science & Business Media, 2012.

71. O. Sagi, L. Rokach, Ensemble learning: A survey. *WIREs Data Min. Knowl.* **8**, e1249 (2018).

72. S. H. Jeong, S. Zhang, K. Hjort, J. Hilborn, Z. Wu, PDMS-based elastomer tuned soft, stretchable, and sticky for epidermal electronics. *Adv. Mater.* **28**, 5830–5836 (2016).